

# A computational approach to curvature sensing in lipid bilayers

Federico Elías-Wolff

Academic dissertation for the Degree of Doctor of Philosophy in Biophysics at Stockholm University to be publicly defended on Friday 7 September 2018 at 14.00 in Magnélisalen, Kemiska övningslaboratoriet, Svante Arrhenius väg 16 B.

## Abstract

Local curvature is a key driving force for spatial organization of cellular membranes, via a phenomenon known as membrane curvature sensing, where the binding energy of membrane associated macromolecules depends on the local membrane shape. However, the microscopic mechanisms of curvature sensing are not well understood. Molecular dynamics simulations offer a powerful complement to biochemical experiments, yet their contribution to the study of curvature sensing has been limited, due in part to the lack of efficient methods, not least because of methodological difficulties in dealing with curved membranes. We develop a method based on simulated buckling, which has been previously employed to study mechanical properties of membranes. Here, we describe, validate and evaluate this method. We then apply to study curvature sensing properties of three model systems, using coarse-grained simulations. On the first system, we study lipid sorting in a three-component lipid mixture with emphasis on cardiolipin. We find that if curvature is high, curvature sensing is strong enough to drive cardiolipin molecules to negative curvature regions, outcompeting other lipids, without the need of external interactions or cooperative effects. We then simulated three systems consisting of a short amphipathic peptide attached to the surface of a buckled membrane. All three peptides localize to positive curvature, in agreement with the so-called cylindrical hydrophobic insertion mechanism. Their orientational preferences, however, defy the prediction of alignment perpendicular to the direction of maximum curvature. They also fail to show expected symmetries, indicating there is more to the picture than purely shape-based effects. The curvature sensing probe of the next system is a transmembrane trimeric protein, which shows preference to intermediate curvature, in agreement with theoretical predictions. But the lack of an expected 2-fold rotation symmetry indicates that the trimer senses the local curvature gradient, and not just the point-wise local curvature. Finally, dispensing with the buckling methodology, we simulated a series of symmetric transmembrane multimers embedded in cylindrical bilayers. Based on the results of these simulations and theoretical arguments, we discuss the relationship between structural symmetry and curvature sensitivity. We conclude that anisotropic (i.e. orientation-dependent) curvature sensing is strongly limited by odd and high order rotational symmetries. However, measurements of in-plane orientation on peptides and asymmetric proteins, as well as dimers and tetramers, should yield valuable information. Our method, along with our initial conclusions, provides an useful tool for the understanding of the relationship between membrane shape and membrane protein function, and should prove useful to biophysicists in the design and interpretation of experimental curvature sensing assays.

**Keywords:** *curvature sensing, membrane curvature, cardiolipin, amphipathic helix, symmetric multimers, lipid bilayer, molecular dynamics.*

Stockholm 2018

<http://urn.kb.se/resolve?urn=urn:nbn:se:su:diva-157417>

ISBN 978-91-7797-332-4  
ISBN 978-91-7797-333-1



**Department of Biochemistry and Biophysics**

Stockholm University, 106 91 Stockholm



A COMPUTATIONAL APPROACH TO CURVATURE SENSING IN  
LIPID BILAYERS

Federico Elías-Wolff





# A computational approach to curvature sensing in lipid bilayers

Federico Elías-Wolff

©Federico Elías-Wolff, Stockholm University 2018

ISBN print 978-91-7797-332-4

ISBN PDF 978-91-7797-333-1

Printed in Sweden by Universitetservice US-AB, Stockholm 2018

Distributor: Department of Biochemistry and Biophysics, Stockholm University

# List of Papers

The following papers, referred to in the text by their Roman numerals, are included in this thesis.

PAPER I: **Computing curvature sensitivity of biomolecules in membranes by simulated buckling**

F. Elías-Wolff, M. Lindén, A.P. Lyubartsev, and E.G. Brandt  
*J. Chem. Theory Comput.*, **14**, 1643-1655 (2018).

DOI: 10.1021/acs.jctc.7b00878

PAPER II: **Curvature sensing by cardiolipin in a simulated buckled membrane**

F. Elías-Wolff, M. Lindén, A.P. Lyubartsev, and E.G. Brandt  
*Submitted* (2018).

PAPER III: **Anisotropic membrane curvature sensing by amphipathic peptides**

J. Gómez-Llobregat, F. Elías-Wolff, and M. Lindén  
*Biophys. J.*, **110**, 197-204 (2016).

DOI: 10.1016/j.bpj.2015.11.3512

PAPER IV: **Curvature sensing by multimeric proteins**

M. Lindén, F. Elías-Wolff, A.P. Lyubartsev, and E.G. Brandt  
*Manuscript in preparation*

---

Reprints were made with permission from the publishers.

The following is a list of papers by the author not included in this thesis.

PAPER V: **Metapopulation dynamics on the brink of extinction**

A. Eriksson, F. Elías-Wolff, and B. Mehlig *Theor. Popul. Biol.*, **83**, 101-122 (2013).

DOI: 10.1016/j.tpb.2012.08.001

PAPER VI: **The emergence of the rescue effect from explicit within- and between-patch dynamics in a metapopulation**

A. Eriksson, F. Elías-Wolff, B. Mehlig, and A. Manica *Proc. R. Soc. B*, **281**, 20133127 (2014).

DOI: 10.1098/rspb.2013.3127

PAPER VII: **How Levins' dynamics emerges from a Ricker metapopulation model**

F. Elías-Wolff, A. Eriksson, A. Manica, and B. Mehlig *Theor. Ecol.*, **9**, 173-183 (2016).

DOI: 10.1007/s12080-015-0271-y

# Abbreviations

<b>ACS</b>	American Chemical Society
<b>CG</b>	coarse-grained
<b>CL</b>	cardiolipin
<b>FENE</b>	finite extensible nonlinear elastic
<b>lipB</b>	big-headed Cooke lipid
<b>lipC</b>	cylindrical Cooke lipid
<b>lipS</b>	small-headed Cooke lipid
<b>MD</b>	molecular dynamics
<b>PME</b>	particle mesh Ewald
<b>POPE</b>	1-palmitoyl-2-oleoyl phosphatidylethanolamine
<b>POPG</b>	1-palmitoyl-2-oleoyl phosphatidylglycerol
<b>RMSD</b>	root-mean-square deviation



# Contents

<b>1</b>	<b>Introduction</b>	<b>1</b>
<b>2</b>	<b>Lipid bilayers</b>	<b>3</b>
2.1	Elasticity of cell membranes . . . . .	4
2.2	Cardiolipin as a curvature sensor in lipid membranes . .	6
<b>3</b>	<b>Curvature sensing</b>	<b>9</b>
3.1	Curvature sensing and generation mechanisms . . . . .	10
3.2	Curvature sensing experiments . . . . .	10
<b>4</b>	<b>Molecular dynamics</b>	<b>13</b>
4.1	Coarse-grained models . . . . .	14
4.1.1	The Cooke lipid model . . . . .	15
4.1.2	The Martini force field . . . . .	16
<b>5</b>	<b>Simulated buckling (I)</b>	<b>19</b>
5.1	Frame alignment . . . . .	20
5.2	Orientation Analysis . . . . .	22
5.3	Method evaluation . . . . .	23
<b>6</b>	<b>Lipid Sorting (I,II)</b>	<b>27</b>
6.1	Geometric effects of curvature on lipid packing . . . . .	27
6.2	Curvature-dependent lipid distribution and structure . .	30
6.3	Theoretical analysis of lipid sorting for two- and three- component bilayers . . . . .	33
<b>7</b>	<b>Curvature sensing by proteins and peptides (I,III,IV)</b>	<b>39</b>
7.1	Position- and orientation-dependent curvature sensing .	39
7.2	Trimer in a buckled membrane (Paper I) . . . . .	43
7.3	Amphipathic helices in a buckled membrane (Paper III) .	44
7.4	Symmetric proteins in cylindrical bilayers (Paper IV) . .	47

<b>8 Conclusions</b>	<b>55</b>
<b>Appendix A Autocorrelation times</b>	<b>59</b>
<b>Sammanfattning</b>	<b>lxi</b>
<b>Acknowledgements</b>	<b>lxiii</b>
<b>References</b>	<b>lxv</b>

# 1. Introduction

How do cells create and maintain their geometry? This is one of the central questions in cell biology. For many cellular processes, the associated machinery of the cell needs to be recruited to the proper place at specific times. For example, during endocytosis (a cellular process where the cell absorbs a molecule by engulfing it) appropriate concentrations of certain membrane lipids and proteins need to be present at the site of absorption in order to form the engulfing vesicle. What is the mechanism by which these biomolecules localize to the specific membrane region?

The ancients saw the cell membrane as a lipid barrier with selective permeability. The modern picture is far more complex. Membrane proteins typically constitute about 50% of the membrane volume. Each of these proteins performs some biological activity, including the passive or active transport of molecules which are involved in the cell's metabolism, in the communication of the cell with other cells, among many others. While some of these functions can happen anywhere in the membrane and thus the associated proteins are distributed all over it (for example proteins acting as mechanosensitive channels that let water out when the cell's internal pressure is too high), others require the localization of the corresponding proteins to a specific region, for examples during cell division or endocytosis mentioned above.

Several mechanisms are responsible for localizing biomolecules to appropriate regions within cells. One of these mechanisms is the sensing of membrane curvature by proteins and other biomolecules, that is, by expressing a positional preference for membrane regions within a certain range of local curvature. In this project we study how membrane proteins and lipids interact to sense the shape of lipid membranes. Thus, we develop a novel computational method based on molecular dynamics simulations of buckled membranes. The basic idea is to construct a lipid bilayer, compress it so it acquires a buckled shape with known curvature parameters, and observe how probe molecules, like an embedded peptide, or a particular lipid species, prefer a certain

curved regions within the bilayer patch. For pure lipid membranes, we develop a simple theory, based on the Helfrich model of cell membrane elasticity, to describe how lipids sort themselves between curvature regions. When we consider the localization of peptides and membrane proteins, not only the position but also the orientation of the molecules becomes relevant. Similarly, we propose a phenomenological model to describe the curvature sensing properties of the peptides, in terms of position- and direction-dependent curvature. In addition to tracking the joint distribution of position and orientation along buckled membranes, we also simulate multimeric model proteins in cylindrical membrane patches, where only the orientation is relevant. For this case we develop a theory to explain why monomeric, dimeric and tetrameric protein models have much stronger orientational preferences than their trimeric, pentameric and hexameric analogues.

The main focus of this research are the mechanisms by which proteins and lipids induce and regulate the spatial organization of the cell membrane. The principal questions we attempt to investigate can be formulated in terms of the curvature dependent free energy of the systems we study. What is the shape of the free energy landscape for distinct types of curvature sensing molecules? How does the shape asymmetry of these peptides, which brings an orientational dependence on the binding energy, affect the free energy landscape? We thus test if the orientation of curvature sensors corresponds to theoretical predictions of the corresponding curvature sensing mechanisms. Our first goal is to develop a computational method that is fast and accurate, and ideally suited to answer these questions.

Aside from the intrinsic interest associated with the study of curvature sensing and generation, and the identification of its underlying mechanisms, our method should provide a novel tool in membrane biophysics, which complements existing approaches. Particular applications include finding the orientational preferences of key membrane peptides, and the examination of adsorption of biomolecules or nanoparticles in curved interfaces. This, we hope, will promote the development of experimental techniques to tackle these issues. On the side of medical applications, we believe that deeper understanding of the interplay between antimicrobial peptides, as described above, will prove useful in antibiotic development.

## 2. Lipid bilayers

Biological bilayers are composed of amphiphilic phospholipids, which typically consist of two hydrophobic fatty acid tails, a hydrophilic phosphate head. Lipids dissolved in water self-assemble into quasi two dimensional aggregates known as lipid bilayers, which are the simplest and main structural component of cellular membranes, including the plasma membrane, the vesicles used in cell-cell communication and viruses, organelle membranes, and other subcellular structures. As Fig. 2.1 illustrates, membranes in cells are highly complex and highly dynamic structures, containing a variety of lipid species, many kinds of surface bound, and transmembrane proteins, and sterols. However, in vitro experiments and computer simulations often deal with simplified membrane models which contain a reduced variety of lipid components, and only a few proteins.

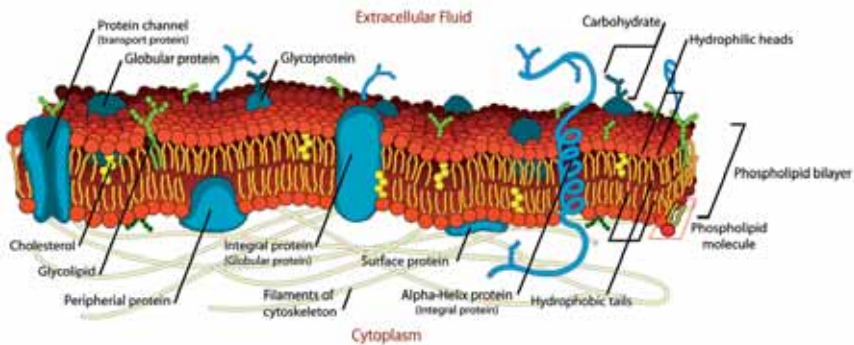


**Figure 2.1:** Schematic picture of a cell membrane patch (Figure credit: Mariana Ruiz, Wikimedia Commons, public domain)

Lipid bilayer patches with lateral length scales only a few times the height of a lipid molecule are remarkably well described by continuum models with a very small number of parameters (the material constants). A few theoretical models have been developed to describe curvature sensing. These include theories based on Helfrich-type or Leibler-type free energy functionals, and the bending stiffness model,

as well as thermodynamic models fitted to experimental observations [1]. Typically, continuum models rely on a second order expansion of the local coupling. Specifically, the bilayer is modeled by an energy functional quadratic in the local curvature tensor elements. These kinds of models have their shortcomings though. Quadratic theories imply intrinsic curvature preferences which have proven hard to experimentally observe, as in almost all experimental curvature sensing assays, curvature sensors localize to the maximal curvature available to them [2–4]. Experimental observation of this phenomena, where the sensors actually show a preference for intermediate curvature within an assay, is very scarce, but two examples were shown in Refs. [5, 6]. Continuum models have been shown to underpredict induced curvature [7]. Quadratic theories also imply certain symmetries [1]. In Chapter 7 we show that some of these expected symmetries are violated in our simulated systems, and we discuss the implications to curvature sensing phenomena.

## 2.1 Elasticity of cell membranes

A buckled bilayer geometry is likely inaccessible in experiments, however, it offers several pragmatic advantages in simulations. Namely, it presents a continuous range of curvature including both positive and negative curvature in both leaflets (thus lipids can access curvature of either sign without the need of lipid flip-flops), and a curved structure with high curvatures can be constructed with a small number of lipids. To provide a mathematical description of a buckled lipid bilayer, in this section, we follow the derivation presented in Ref. 8. The curvature energy of a lipid bilayer can be expressed by a functional  $F$  of the surface shape  $S$ ,

$$F[S] = \int_S dA \left( \frac{1}{2} \kappa (K(S) - K_0)^2 + \tilde{\kappa} K_G(S) \right), \quad (2.1)$$

where  $\kappa$  is the mean curvature modulus,  $\tilde{\kappa}$  is the Gaussian curvature modulus,  $K$  the total curvature (the sum of the two local principal curvatures),  $K_0$  the spontaneous curvature, and  $K_G$  the Gaussian curvature (the product of the two principal curvatures). Equation (2.1) is known as the Helfrich functional [9]. Due to the Gauss-Bonnet theorem [10], the contribution from Gaussian curvature is constant if the buckled membrane is a periodic surface with constant topology.

A buckled membrane can be obtained by lateral compression of a flat bilayer patch. This is the two dimensional analogue of compressing an elastic rod, a problem known as the Euler elastica [11]. In terms of the functional  $F[S]$ , we can achieve this by adding a constraint term which fixes the projected length along the membrane's long axis, which we set as the  $x$ -axis, while at the same time, parameterizing the surface in terms of the bilayer's tangent angle  $\psi$  (Fig. 2.2). Eq. (2.1) thus becomes

$$F[\psi] = L_y \int_0^L ds' \left( \frac{1}{2} \kappa \psi^2 + \lambda \left( \cos \psi - \frac{L_x}{L} \right) \right) \quad (2.2)$$

where  $L$  is the length of the bilayer along the buckle,  $L_x$  the projected length on the  $x$ -axis, and  $\lambda$  is a Lagrange multiplier that fixes  $L_x$ . We describe the buckled shape in terms of a normalized arc length parameter  $s = s'/L$  ( $0 \leq s \leq 1$ ), so that  $K = \psi'(s)/L$ , and the projected length is  $L_x = L \int_0^1 ds \cos(\psi(s))$ . The shape of the buckled bilayer is obtained by minimizing  $F$ , with fixed  $L_x$ . The Euler-Lagrange equation yields

$$\frac{\partial^2 \psi(s)}{\partial s^2} = -\lambda_L \sin(\psi(s)), \quad (2.3)$$

where  $\lambda_L$  is a Lagrange multiplier that has absorbed the bending modulus  $\kappa$ . Equation (2.3) can be solved analytically, and the solution is given in terms of Jacobi elliptic functions in Ref. [8, 12]. To avoid handling special functions, we follow a different route. We solve Eq. (2.3) numerically for  $\psi(s)$  (using Matlab's boundary problem solver) with the boundary conditions

$$\psi(0) = \psi(L) = 0, \quad X(0) = Z(0) = Z(L) = 0, \quad X(L) = L_x, \quad (2.4)$$

and obtain the buckled shape in Cartesian coordinates

$$X(s) = \int_0^s d\sigma \cos(\psi(\sigma)), \quad (2.5)$$

$$Z(s) = \int_0^s d\sigma \sin(\psi(\sigma)). \quad (2.6)$$

The buckle shape  $(X(s), Z(s))$  is symmetric:  $X(s) - sL_x$  has period  $1/2$ , is even around  $s = 0$ , and odd around  $s = 0.25$ ;  $Z(s)$  has period  $1$ , is even around  $s = 0.5$  and odd around  $s = 0.25$ . Thus the buckled shape can be accurately approximated by a Fourier series with many zero terms due to the symmetries, as we discuss in Paper I. The Fourier

representation of the buckled shape is given by

$$\begin{aligned} X_M(s, \gamma) &= L_x \left[ s + \sum_{n=1}^M a_n^{(x)}(\gamma) \sin(4\pi ns) \right], \\ Z_M(s, \gamma) &= L_x \left[ a_0^{(z)}(\gamma) + \sum_{n=1}^M a_n^{(z)}(\gamma) \cos(2\pi(2n-1)s) \right], \end{aligned} \quad (2.7)$$

where

$$\gamma = 1 - \frac{L_x}{L}, \quad (2.8)$$

is the compression factor ( $\gamma = 0$  indicates a flat bilayer). The coefficients  $a_n^{(x)}(\gamma)$ ,  $a_n^{(z)}(\gamma)$  in Eq. (2.7) are computed through a least-squares fit to the numerical solution Eq. (2.5).

In Chapter 5, we describe a procedure to align the frames of a resulting trajectory in a simulated buckled bilayer. This procedure requires the repeated evaluation of  $X(s)$  and  $Z(s)$ . For fast evaluation, we construct lookup tables for  $a_n^{(x)}(\gamma)$ ,  $a_n^{(z)}(\gamma)$  in the range  $0 \leq \gamma \leq 0.85$  (for higher values of  $\gamma$ , the buckled bilayer intersects itself). For arbitrary values of  $\gamma$ , the coefficients are computed by spline interpolation. These splines can be analytically differentiated, thus derivatives with respect to  $s$  and  $\gamma$  can be efficiently computed during the alignment procedure in Chapter 5. In practical terms, 3 Fourier components are sufficient for moderate values of  $\gamma$ , while 7 Fourier components are required for precision of at least 5 significant digits for large compression values.

The local curvature of the buckled shape is given by the standard formula

$$K(s) = \frac{Z'(s)X''(s) - X'(s)Z''(s)}{(X'(s)^2 + Z'(s)^2)^{3/2}}, \quad (2.9)$$

with the sign convention that the curvature is positive if the membrane bends away from the probe, that is, for a probe in the upper monolayer, the curvature is positive if the membrane is locally concave (in Fig. 2.2, the curvature is positive at the position of the probe). For transmembrane probes, we take the perspective of the upper monolayer.

## 2.2 Cardiolipin as a curvature sensor in lipid membranes

Cardiolipin (CL) is the signature lipid in mitochondria, where it constitutes 10-20% of mitochondrial membranes [13]. It is also found in

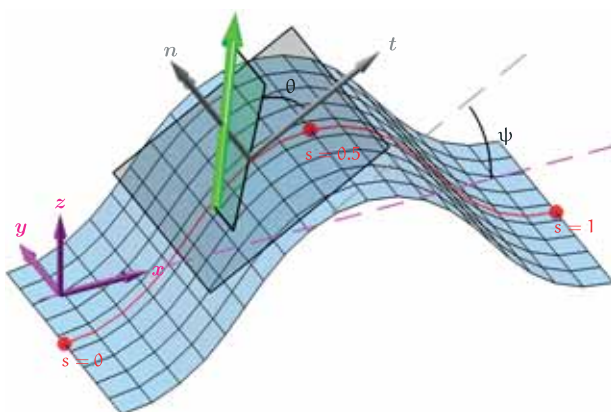


**Figure 2.2:** Schematic representation of a buckled membrane with a bound probe molecule (green arrow). The position of the probe along the buckle is described by the normalized arc length parameter  $s$  (red), and corresponds to the probe’s center of mass, projected to the membrane midplane (blue surface). The angle  $\psi$  corresponds to the angle formed by the  $x$ -axis and the tangential angle  $t$ . The orientation angle  $\theta$  is that between  $t$  and the projection of the peptide’s backbone to the tangential plane. Adapted with permission from Paper I. © 2018 ACS.

bacterial membranes, at 5-10% concentration [14]. The special structure of CL, essentially two phosphatidylglycerol lipid molecules joined together via their phosphate head groups, gives it a distinctly conical shape, making it a relatively strong curvature sensor among phospholipids. For this reason, in Chapter 6, where we study redistribution of lipids in terms of curvature, we pay special attention to cardiolipin, present in simulated buckled bilayers mimicking *E. Coli* lipid composition.

The curvature preferences of CL are also of general interest since CL deficiency is associated with numerous diseases [15–18], and it is believed that CL stabilizes respiratory chain complexes in mitochondrial membranes, and plays a role for proton transport along the mitochondrial membrane surface [19–21]. ATP synthase, which synthesizes ATP using energy released via transmembrane proton transport, associates with the highly curved edges of the mitochondrial membrane cristae [22], where the high curvature might also promote local enrichment of CL. In bacterial membranes, CL has been shown to localize to the curved poles of rod-shaped bacteria [23], and to promote polar localiza-

tion of certain membrane proteins [24, 25]. An elegant theory of how cardiolipin, above certain critical concentration, forms microdomains that localize in the cell poles through cell-wall mediated interactions is presented in [26]. These same results were obtained through numerical simulations in [27]. The effects of cardiolipin localization have important consequences, for example, in the membrane insertion of antimicrobial peptides [28] or amphipathic helices in general [29].

### 3. Curvature sensing

Recently, substantial efforts have been made in the study of the spatial organization of lipids and proteins within the cell membrane. Membrane curvature is increasingly recognized as an important factor for cellular organization and membrane protein function [1, 30–34].

Curvature sensing and curvature generation are intrinsically linked, as both are essentially a response to the same condition: mismatch between local membrane shape and the three dimensional structure of the membrane-bound biomolecules in question. A curvature sensing molecule lowers its curvature-dependent binding energy by localizing to a more convenient membrane region. If the energetics are high enough, curvature sensing molecules can induce membrane deformations for the same purpose. These deformations, however, need to be paid with bending energy (for simulated membranes, this also implies additional bending energy to compensate for the initial deformation so that periodic boundaries are respected), and the energy decomposition between the two phenomena is non-trivial. It is therefore more computationally tractable to provide a pre-curved membrane and follow curvature sensing exclusively, which is the approach we take in the following chapters.

Understanding the mechanisms for curvature sensing and generation should prove useful for medical applications and drug design, as many diseases are associated with curvature sensing proteins. Just one example, Endophilin-B1 is a BAR-domain protein involved in autophagy, whose malfunction is implicated in neurodegenerative, cardiovascular and neoplastic diseases [35]. Furthermore, synthetic biology offers novel avenues for curvature sensing applications. Membrane protein mimics built using DNA nanostructures (with some added hydrophobic molecules so that the DNA constructs can insert into the membrane) can perform biological functions [36]. Since it is easier to design their three dimensional shape than it is for polypeptides, engineered curvature sensing could play an important role in the design of membrane devices.

### 3.1 Curvature sensing and generation mechanisms

Membrane curvature is generated through complex interactions between lipids, membranes and other physical forces, like interactions with the cytoskeleton, with the hydrodynamic flow, or through contact with other membranes or substrates [31]. Several curvature sensing and generation mechanisms are now recognized. These include hydrophilic protein domains on the surface (scaffolding), hydrophobic protein domain insertion (wedging) [1], steric interactions (crowding) [37], and membrane protein oligomerization [38]. In intracellular organelles the first two appear to be the most effective [38].

The interaction between lipids and membrane curvature is more subtle, because the small area per lipid molecule (compared to many proteins) generally prohibits efficient curvature localisation of individual lipid molecules for entropic reasons [39–42]. In principle, lipids can generate membrane curvature if the monolayers are very asymmetrical, with one monolayer having many non-bilayer lipids mixed in, this is however unlikely [32]. Nevertheless, lipids can show significant curvature sensing and generating effects through cooperative effects. Lipid packing defects, small membrane surface areas where the hydrophobic bilayer core is exposed, can arise from membrane bending. Thus localization of membrane proteins so that they cover such defects are favoured [29, 43]. Some proteins bind preferentially to membrane regions enriched with a particular lipid [41]. Interaction between lipid domains and the cell wall may also be significant [23, 26].

### 3.2 Curvature sensing experiments

The majority of principles for production of membrane shape were discovered in experiments of clathrin-mediated endocytosis [32]. Experimental studies of curvature sensing by lipids and proteins use various methods to create a membrane structure with a range of curvatures, and then measure how the molecule of interest partitions between different curvatures [1]. These experiments have identified several proteins that can both sense and generate curvature. These include membrane associated proteins such BAR domains [2, 44–49], various amphipathic and antimicrobial peptides, [4, 50–53], as well as transmembrane proteins [22, 54–57].

Curvature partitioning assays between vesicles and tubes show that

several kinds of proteins strongly localize to high curvature domains [1]. N-BAR domains cause strong deformations, and usually induce the formation of tubules [58]. The strength of curvature sensing on tube structures depends on protein density. Amphiphysin 1, (N-BAR domain) binds to highly curved membranes and triggers deformations [44]. Dynamin-like proteins are the only known proteins known to mechanically drive membrane fission. By pulling a tubule from a giant unilamellar vesicle, using optical tweezers, and measuring the force required to hold the tube, the force generated by dynamin polymerization can be deduced (18 pN). This force is enough to deform membranes but still can be counteracted by membrane tension [59].

These approaches face several experimental challenges. One is that it is difficult to ensure that the properties of the curvature sensor, or the surrounding membrane, are not influenced by the dye or other additives [60]. There are experimental difficulties to study sensors for high curvatures *in vivo*. Total internal reflection fluorescence microscopy offers good resolution but is only applicable to the plasma membrane. It is also difficult to study low curvatures *in vitro* (it is straightforward for large positive curvatures, more difficult for weak positive curvatures, and very difficult for negative curvatures) [61]. In the case of supported lipid bilayers [46, 62], care must also be taken to minimize unwanted interactions with the supporting surface. Finally, localisation with fluorescence microscopy generally does not provide much details beyond the position and local density of the fluorescent labels [63], and hence give only indirect information about the structural basis of curvature sensing.



## 4. Molecular dynamics

Molecular dynamics (MD) is a computer simulation technique, in which the simulated system evolves by numerically solving Newton's equations of motion for each particle (atom or molecule) of the system, where the forces are defined by intermolecular potentials. These potentials describe all the particle interactions, that is, the bonded interactions and non-bonded interactions including electrostatic and Van der Waals interactions. A typical potential has the form

$$\begin{aligned} U = & \sum_{\text{bonds}} k_b(\mathbf{r} - \mathbf{r}_0)^2 + \sum_{\text{angles}} k_a(\theta - \theta_0)^2 + \sum_{\text{torsions}} k_d(1 + \cos(n\phi - \delta)) \\ & + \sum_{i,j \neq i} 4\epsilon_{ij} \left[ \left( \frac{\sigma_{ij}}{r_{ij}} \right)^{12} - \left( \frac{\sigma_{ij}}{r_{ij}} \right)^6 \right] + \sum_{i,j \neq i} \frac{q_i q_j}{\epsilon r_{ij}}, \end{aligned} \quad (4.1)$$

where the first three terms correspond to the bonded interactions (bond stretching, angle bending and torsions), the fourth term describes Van der Waals interactions (by means of a Lennard-Jones potential), and the last term corresponds to the Coulombic interactions. Functions such as Eq. (4.1), along with the values of the parameters ( $k_b$ ,  $k_a$ ,  $k_d$ ,  $r_0$ ,  $\theta_0$ ,  $n$ ,  $\delta$ ,  $\epsilon_{ij}$ ,  $\sigma_{ij}$ ,  $q_i$ ,  $q_j$ ) for each kind of particle (be it an atom, or a coarse-grained interaction site), form what is known as a force field. The values of these parameters can be derived from quantum mechanical calculations, by fitting statistics from simulations to physical and chemical experiments or a combination of both.

In this project, all molecular dynamics simulations were performed using the Gromacs software [64, 65], and employing two different coarse grained force fields known as the Cooke and Martini models, detailed description of which is given below. In paper I we developed the buckling method employing the Cooke model, which represents lipids with only three coarse grained beads, allowing for very fast computations. In papers II and III we used the buckling method while employing the Martini force field, where the lipids we used are represented by 13 coarse grained beads (25 for cardiolipin), and unlike for the Cooke

model, explicit solvent is also simulated with coarse grained water molecules.<sup>1</sup> Although the computational requirements are much greater than for the Cooke model, the Martini model is still several orders of magnitude faster than atomistic simulations, while retaining much molecular detail and is thus amenable to semiquantitative physical interpretation. In paper IV we return to the Cooke model, but do away with simulated buckling, instead simulating model multimers in cylindrical bilayers, where the curvature free energy is dependent only on orientation.

The trajectory alignment was performed by a custom module for PLUMED [66], written in C++ and using the dlib library for linear algebra and non-linear optimizations [67]. The statistical analysis was performed in MATLAB [68], and VMD was used for graphical visualization of simulated trajectories [69].

## 4.1 Coarse-grained models

Additional challenges are present in MD simulations. One of the most obvious is that for systems containing a large number of atoms, MD may prove to be too computationally expensive. Several approaches exist to deal with this situation. Coarse-graining is an approach where the system is described by so called coarse-grained beads, each representing a group of atoms and its collective behaviour. This approach can speed-up simulations by several orders of magnitude, while still retaining significant molecular detail, but carries along its own limitations. Forcefields for a particular coarse-grained approach are generally non transferable to simulation settings which are different from the setting for which it was developed. Another fundamental limitation of note comes in the form of the balance between enthalpy and entropy. As the degrees of freedom in a CG description are reduced so is the entropy, which is compensated by reduced enthalpy terms. Thus, while free energy differences may be accurate, free energy decomposition is not possible.

<sup>1</sup>For reference, POPE has 125 atoms (76 of which are hydrogen), POPG has 128 atoms (77 hydrogen), and the cardiolipin molecule we employ contains 242 atoms (146 hydrogen).

### 4.1.1 The Cooke lipid model

The solvent-free Cooke model represents lipids with three beads [70]. The units of length, energy and time in the Cooke model are  $\sigma$ ,  $\varepsilon$ , and  $\tau$ , respectively. The sizes of the lipid beads are determined by the parameter  $b$  in a Weeks-Chandler-Andersen potential[71]

$$V_{\text{WCA}}(r) = \begin{cases} 4\varepsilon \left[ (b/r)^{12} - (b/r)^6 + \frac{1}{4} \right], & r \leq r_c \\ 0, & r > r_c, \end{cases} \quad (4.2)$$

with  $r_c = 2^{1/6}b$ . Values of  $b_{\text{head,head}} = b_{\text{head,tail}} = 0.95\sigma$  and  $b_{\text{tail,tail}} = \sigma$ , give the lipids an effective cylindrical shape [72]. The two bonds in a lipid are modeled with a finite extensible nonlinear elastic (FENE) potential

$$V_{\text{bond}}(r) = -\frac{1}{2}k_{\text{bond}}r_{\infty}^2 \log [1 - (r/r_{\infty})^2], \quad (4.3)$$

with values for stiffness  $k_{\text{bond}} = 30\varepsilon/\sigma^2$  and divergence length  $r_{\infty} = 1.5\sigma$ . Lipids are kept straight by means of a harmonic potential between the first and third beads, with equilibrium length  $4\sigma$  and bending stiffness  $10\varepsilon/\sigma^2$ .

In lieu of solvent particles, hydrophobicity is mimicked by a long-range attractive potential between tail beads:

$$V_{\text{cos}}(r) = \begin{cases} -\varepsilon, & r < r_c \\ -\varepsilon \cos^2 \frac{\pi(r-r_c)}{2w_c}, & r_c \leq r \leq r_c + w_c \\ 0, & r > r_c + w_c. \end{cases} \quad (4.4)$$

The potential (4.4) has a decay range parameter set to  $w_c = 1.6\sigma$ . In all our simulations with the Cooke model, the temperature is set to  $k_B T = 1.08\varepsilon$ . This combination of  $w_c$  and  $T$  yields a stable fluid bilayer phase [72]. Cooke simulations were run at constant volume, using the leap-frog stochastic dynamics integrator with time step of  $0.01\tau$ . The friction constant, which defines the time scale, is  $\Gamma = \tau^{-1}$ . All CG beads are electrically neutral.

The model reproduces bilayer self-assembly, phospholipid phase diagrams and elastic properties that are qualitatively correct [72]. Of course, such a highly coarse-grained model has its disadvantages. In particular, the Cooke model introduces some peculiar behaviour including an artificially high lipid flip-flop rate, and a tendency for individual lipids to detach from the bilayer and wander around the simulation box (i.e. going into gas phase) for a limited time before returning

into the bilayer. About 1% of lipids can be found in this gas phase at any given time [70].

Based on typical values of bilayer thickness and lipid diffusion, the mapping of length and time scales are roughly given by  $\sigma \approx 1$  nm, and  $\tau \approx 10$  ns [70].

#### 4.1.2 The Martini force field

Martini [73–76] is based on a mapping of 4 heavy atoms, along with their associated hydrogens, to one CG bead, of which four types are defined: polar, apolar, non-polar and charged. The force field provides a speed-up of several orders of magnitude compared to atomistic simulations, while still retaining significant molecular detail. For the parameterization of Martini, bonded interactions were derived from atomistic simulations, while non-bonded interactions were fitted to reproduce partitioning free energies from experiments. Martini has been heavily tested and validated against biomolecular systems, and it is known to accurately reproduce the elastic properties of lipid bilayers. In particular, the Martini force field has proven very successful in the simulation of membrane-protein lipid interplay, for example the domain partitioning of membrane peptides, or the prediction of binding modes of proteins to membranes. Martini topologies are available for many lipids and surfactant molecules, all amino acids, and several sugars, nanoparticles and polymers. Topologies can also be easily constructed for arbitrary proteins and peptides from available software. These require addition of elastic networks that constrain secondary structure.

All our Martini simulations were run at constant temperature of 300 K using the Bussi velocity-rescaling thermostat [77] with coupling constant of 1 ps. Pressure was maintained at 1 bar with semiisotropic coupling and 12 ps time constant, using the Parrinello-Rahman barostat, and with constant xy area. Electrostatics were handled with the PME method [78]. The time step was set at 25 fs.

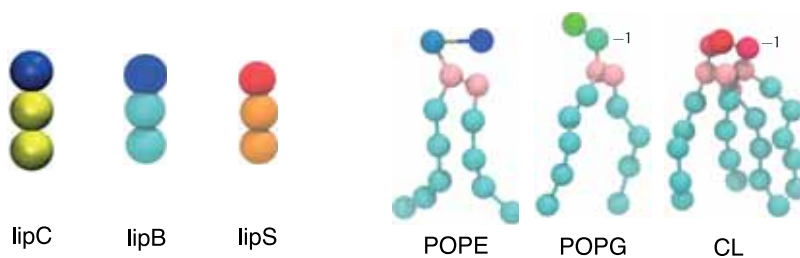


**Figure 4.1:** Representation of lipids investigated in this work. On the left, Cooke lipids with to cylindrical shape (lipC), big headed lipid (lipB) and small headed lipid (lipS). On the right, Martini representations of 1-palmitoyl-2-oleoyl phosphatidylethanolamine (POPE), 1-palmitoyl-2-oleoyl phosphatidylglycerol(-1) (POPG) and cardiolipin(-1) (CL), annotated with the head group charges. Left panel adapted with permission from Paper I. © 2018 ACS. Right panel adapted from Paper II.



# 5. Simulated buckling (I)

In Paper I, we develop a computational method to study curvature sensing based on simulated buckling. This chapter gives a description and evaluation of the method, though some of the results reported in Paper I are deferred to Chapter 6 (namely Sections 3.2 and 3.3 in the paper), and to Chapter 7 (Section 3.4).

Computer simulations can provide additional insights into the mechanisms of curvature sensing, but suffer from other kinds of difficulties. Simulations of flat bilayers rely on detecting induced local membrane deformations [22, 53, 79] which can be difficult to interpret. Simulations of bilayers having shapes of spheres [80] or cylinders [81] require equilibration between lipids and solute between the inside and outside of the system, which can be difficult unless very coarse-grained models are used.

Simulated buckling can circumvent some of these difficulties. Yet, another obstacle arises: the buckled shape is subject to strong fluctuations, particularly in the phase of the buckled shape along the compression axis. Thus, in order to be able to collect statistics of positional data, each frame of a simulated buckled bilayer trajectory must be aligned to some reference shape.

To obtain a buckled membrane the following procedure is followed. First, a flat membrane is constructed using a Matlab script for a given number of lipids and  $xy$  aspect ratio. The aspect ratio should be such that even after compression, the projected length  $L_x$  is larger than the length  $L_y$ , otherwise the buckle is subject to orientation transitions, that is, if  $L_x \approx L_y$  the buckle can transition from being along the  $x$  direction to the  $y$  direction, back and forth. This membrane patch is then energy minimized, and a short equilibration is run. Then the membrane patch is compressed along the  $x$  axis by a given buckling factor, by rescaling the  $x$  position of each molecule. If the buckling factor is large, this may be problematic, as some atoms can end up in very high potential energy positions. This problem can be resolved by compressing in stages, and/or by manually relocating the offending atoms. After com-

pression the system is again energy minimized and equilibrated, after which production runs are performed.

Experimental assays [44, 82] have established the curvature preferences of several peptides, as well as lipids, of which cardiolipin, given its particularly conical shape has relatively pronounced intrinsic curvature preference. On the following chapters, we will use our computational method to simulate systems that somewhat mimic these experiments.

In our approach, we simulate a buckled bilayer, which is formed by compressing a flat bilayer along its long axis. This approach provides a profile which is symmetric between monolayers, and gives a continuous range of curvatures.

To filter out phase and length fluctuations in the simulated buckled bilayer, we have developed an alignment procedure, which relies on fitting the surface formed by the lipid's innermost tail beads (the bilayer midplane) to the theoretical buckled shape of a compressed fluid membrane described in Section 2.1. The first step is thus to calculate this theoretical shape. We follow the approach presented in [8] and proceed as follows.

First, the energy of a lipid bilayer can be expressed as a Helfrich-type functional of its surface shape, Eq. (2.1) [9]. Minimization of this energy, with appropriate boundary conditions yields an expression for the theoretical shape of a buckled membrane. We then proceed to fit each simulated frame of the buckled bilayer to this reference shape, by minimizing the mean squared distance from the bilayer mid-plane to the theoretical shape, the parameters of which are the minimization variables. For practical reasons (so that the method can be implemented in reasonable time) the alignment procedure must be both accurate and efficient.

## 5.1 Frame alignment

The theoretical buckled shape  $(X(s; \gamma), Z(s; \gamma))$ , given in Eqs. (2.7), was described in Section 2.1. To align each frame in a simulated trajectory, we fit this curve to the positions, in the  $xz$  plane, of the innermost lipid tail beads, denoted below as  $(x_j, z_j)$  for  $j = 1, \dots, N$ , where  $N$  is the number of beads. The fit is achieved by minimizing the sum of squared

distances,  $\chi^2$ , from these beads to the curve  $(X(s; \gamma), Z(s; \gamma))$

$$\min_{x_0, z_0, \gamma, s_j} \chi^2 = \min_{x_0, z_0, \gamma, s_j} \frac{1}{2} \sum_{j=1}^N (x_0 + X(s_j; \gamma) - x_j)^2 + (z_0 + Z(s_j; \gamma) - z_j)^2. \quad (5.1)$$

The minimization parameters are the offsets  $x_0$  and  $z_0$ , the compression factor  $\gamma$  (since the membrane length  $L$  fluctuates), and the  $s_j$ , corresponding to the projected positions of the innermost tail beads in terms of the normalized arc length  $s$ . As simulations are performed with periodic boundaries, the differences in Eq. (5.1) must adhere to the minimum image convention.

Figure 5.1 shows an aligned frame, together with the fitted buckled shape. Position data along the buckle is described by the parameter  $0 \leq s \leq 1$ .

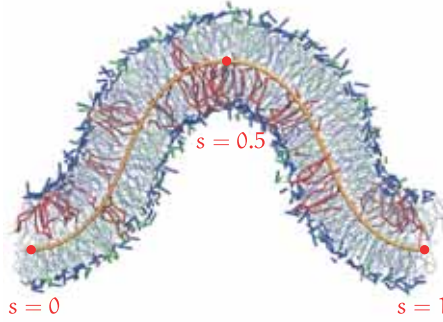


**Figure 5.1:** Snapshot of an aligned buckled membrane. This particular frame corresponds to the **CL12** simulation (Table 6.1), where cardiolipin molecules are shown in red, POPG in green, and POPE in blue. The curve in orange corresponds to the fitted theoretical buckled shape. Positions along the buckle are described in terms of the normalized arc length parameter  $s$  (red). Adapted from Paper II.

Since the fit is strongly nonlinear, good initial conditions are required to ensure fit convergence. We can obtain these by first performing a preliminary fit to a trigonometric function, acting as an approximation to the buckled shape. We define

$$z_j = z_1 + b \sin(2\pi(x_j - x_0)/L_x - \pi/2), \quad (5.2)$$

and fit the innermost tail bead positions  $(x_j, z_j)$  to Eq. (5.2) in the least-squares sense, thus obtaining good estimates to  $x_0$  and  $z_0 = z_1 - |b|$ .

If  $b$  is negative the value of the  $x$ -offset is adjusted to  $x_0 = \text{mod}(x_0 + L_x/2, L_x)$  (where  $\text{mod}$  is the modulo operator). The initial guess for the  $s$ -values of the beads is  $s_j = (x_j - x_0)/L_x$ . For subsequent frames these initial conditions can be taken from the previous fit, thus eliminating the need for the preliminary fit, unless the frames are far apart in time.

Once a frame has been aligned, the position  $s_p$  or the curvature sensing probe needs to be determined. It corresponds to the projection of the probe's center of mass  $(\bar{x}_p, \bar{z}_p)$  to the fitted buckled shape  $(X, Z)$ , obtained through minimization of the squared distance

$$s_p = \arg \min_s (x_0 + X(s, \gamma) - \bar{x}_p)^2 + (z_0 + Z(s, \gamma) - \bar{z}_p)^2. \quad (5.3)$$

## 5.2 Orientation Analysis

The orthogonal Procrustes problem [83, 84]

$$\mathbf{R} = \arg \min_{\Omega} \|\Omega \mathbf{P} - \mathbf{Q}\|, \quad \Omega \in \text{SO}(3), \quad (5.4)$$

where  $\mathbf{Q} = (q_1, \dots, q_N)$  denotes the set of points representing the position of the probe atoms,  $\mathbf{P} = (p_1, \dots, p_N)$  represents the reference probe,  $\|\cdot\|$  denotes the Frobenius norm, and  $\text{SO}(3)$  indicates the 3D rotation group. The solution is the rotation matrix closest to  $\mathbf{M} = \mathbf{Q}\mathbf{P}^T$ . We compute the singular value decomposition  $\mathbf{M} = \mathbf{U}\Sigma\mathbf{V}^T$ , where  $\mathbf{U}$  and  $\mathbf{V}$  are orthogonal matrices, the columns of which contain the left- and right-singular vectors, respectively, and  $\Sigma$  is a  $3 \times 3$  diagonal matrix, containing the singular values of  $\mathbf{M}$ , which are real and non-negative.  $\Sigma$  needs to be modified into a proper rotation matrix  $\Sigma'$  where the smallest singular value is replaced by  $d = \text{sign}(\det(\mathbf{U}\mathbf{V}^T))$ . Finally, the optimal rotation matrix is given by  $\mathbf{R} = \mathbf{U}\Sigma'\mathbf{V}^T$ .

From  $\mathbf{R}$  we compute the Euler angles corresponding to the rotation. Considering the intrinsic rotation sequence  $z - y - z$ , the angles from  $\mathbf{R} = \mathbf{R}_\eta \mathbf{R}_\zeta \mathbf{R}_\xi$  are given by

$$\begin{aligned} \eta &= \text{atan2}(R_{23}, R_{13}) \\ \zeta &= \arccos R_{33} \\ \xi &= \text{atan2}(R_{32}, -R_{31}). \end{aligned} \quad (5.5)$$

where  $R_{ij}$  are matrix elements. If  $\cos \zeta \approx \pm 1$ , the matrix  $\mathbf{R}$  contains only one independent degree of freedom. In this case, we arbitrarily

set  $\eta_{\pm} = 0$  and determine the remaining angle from

$$\xi_{\pm} = \arccos(R_{22}). \quad (5.6)$$

Finally, the orientation angle of the probe molecule is  $\theta = \eta + \xi$ .

### 5.3 Method evaluation

As the alignment procedure is performed for every simulated frame, this procedure needs to be robust and efficient. Here we investigate the stability of the method with respect to two factors, namely the presence of noise, and a decrease in the number of beads used in the fit. First, to evaluate robustness to noise, we perform simulations where, for each frame, a given number of noise beads are added in random positions in the simulation box. The noise level is defined as the number of added noise beads, divided by the number  $N$  of innermost tail beads used in the fit, Eq. (5.1). Second, we reduce the number of optimization parameters in (5.1) by selecting a random subset of the innermost tail beads used for the fit (thus reducing  $N$ ) and evaluate the quality of the fits. We define  $N$  divided by the total number of lipids as the fit resolution. Reducing the fit resolution can lead to significant improvement in computational performance. To validate and evaluate the method described above, we performed simulations of buckled bilayers composed of 1024 Cooke lipids, compressed to a value of  $\gamma = 0.2$  and ran for a time of  $10^7 \tau$ .

Figure 5.2 shows the root mean squared deviation,  $(\chi^2/N)^{1/2}$  as a function of time for a  $10^6 \tau$  slice of a simulated trajectory, where  $N = 256$  were used for the fit, and for two different noise levels. We observe that even for the worst case present, the fit is fairly reasonable.

In addition to the RMSD, we also evaluate the fit in terms of  $s_{\text{error}} = |s - s^*|$ , where  $s^*$  is the fitted value where the noise level is 0%, and the resolution 100%. Figure 5.3 shows both these indicators as functions of the noise level and resolutions in box plots. We observe that for noise levels below 10%, we get RMSD values below  $0.9\sigma$  and  $s_{\text{error}}$  below 0.015 with 98% confidence. Even the worst outliers give errors below 5%, and RMSD of  $1.2\sigma$ , which are reasonable values as Fig. 5.2 indicates. Higher noise levels can introduce bigger deviations, while also affecting performance, as indicated by Fig. 5.4b. Regarding the fit resolution, we see that similar accuracy is achieved with a resolution as

low as 25%. This is a particularly important feature, since we use standard optimization algorithms for the optimization of Eq. (5.1), which scale cubically with  $N$  (Fig. 5.4a). Reducing the resolution further however, not only introduces larger errors, but it also negatively impacts the performance of the method, as the initial fit of each frame fails to converge with increasing frequency. Repeated attempts (with different initial conditions) negatively affect performance, as is clear in Fig. 5.4a for  $N < 250$ .

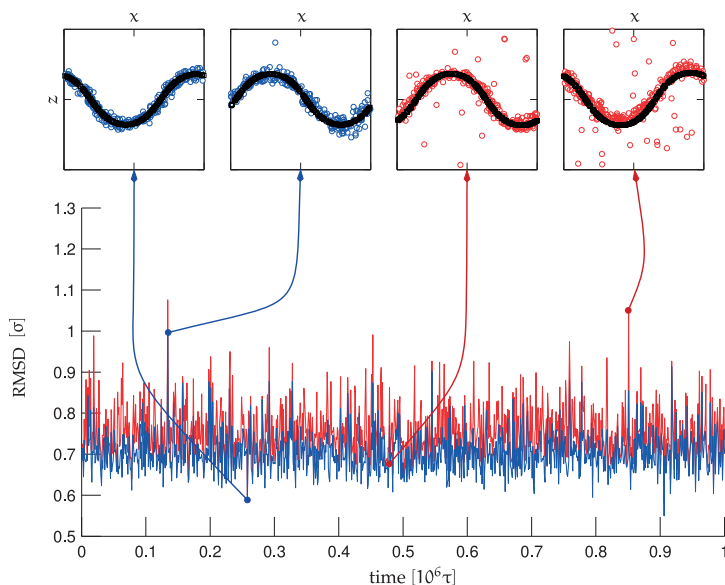


**Figure 5.2:** The root mean squared deviation (RMSD) of the fit to Eq. (5.1) as a function of time. 256 beads were used for the fit, corresponding to resolution of 25%. The blue curve corresponds to a trajectory with no added noise, while the trajectory in red contains 24 added noise beads in each frame. The snapshots correspond to the best and worst fits for each of the noise levels. The black curves are fitted curves, while the colored circles represent the beads used for the fit. The figure shows a trajectory of duration  $10^6\tau$ . Reprinted with permission from Paper I. © 2018 ACS.

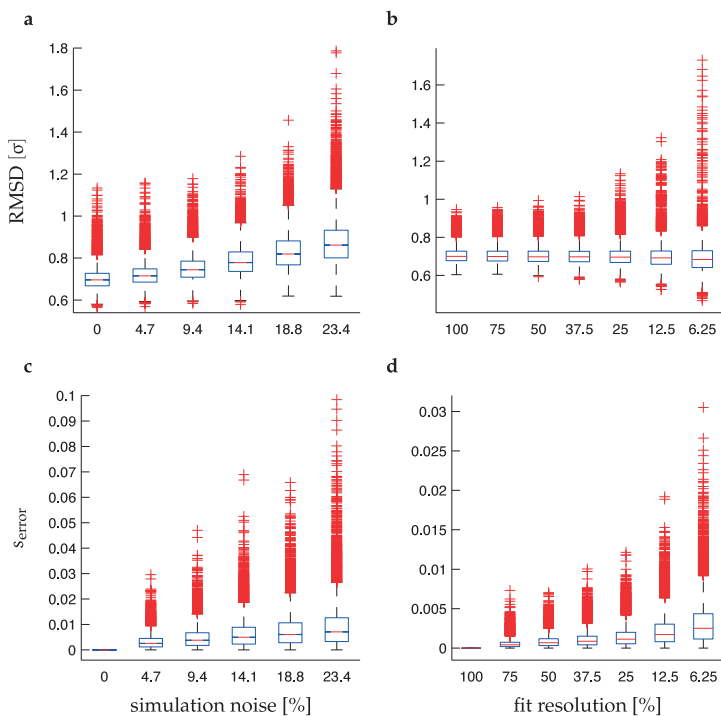


**Figure 5.3:** (a) Box plot of the fitted RMSD as function of noise level (percentage of added noise beads with respect to the number  $N = 256$  of beads used for the fit). (b) RMSD as a function of resolution level indicated by the percentage of innermost tail beads used for the fit. (c–d) Same as panels a,b but for  $s_{\text{error}}$ . The simulated bilayers consist of 1024 lipids, the buckling factor is  $\gamma = 0.2$ , simulation time is  $10^6\tau$ , from which  $2 \times 10^4$  data points were taken. The whisker length is 1.5 times the interquartile range. Reprinted with permission from Paper I. © 2018 ACS..

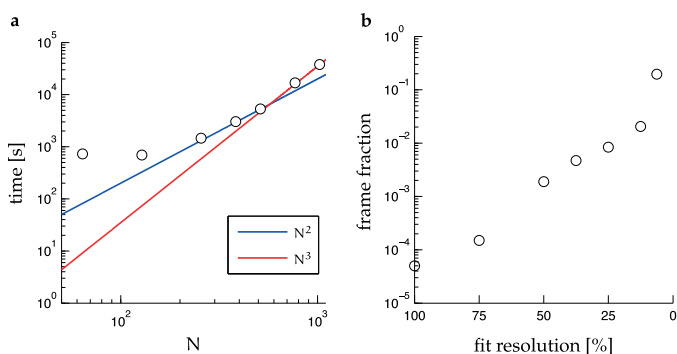


**Figure 5.4:** (a) Computational time (in seconds) as a function of the number of lipids  $N$  used in the frame alignment in a simulation of length  $10^6\tau$ , of a membrane patch with 1024 lipids and  $\gamma = 0.2$ . 20,000 frames were fitted. The red line indicates that the time complexity of the current implementation of the method which is  $O(N^3)$ . The blue line corresponds to  $O(N^2)$  scaling, which is in principle possible, as the Hessian of the objective function (5.1) can be inverted in linear time using Schur decomposition. (b) Fraction of frames in which the initial fit failed to converge, as a function of fit resolution. Adapted with permission from Paper I. © 2018 ACS.

## 6. Lipid Sorting (I,II)

In this chapter we investigate how the spatial distribution of lipids in a membrane is affected by bending it. Curvature sensing effects on lipids are weak, due to the small area footprint of individual lipids. Simulated buckling however, allows for the efficient study of lipid distribution as a function of curvature, as these systems present a continuous range of curvature which can include very high values while simulating small membrane patches. In Paper I we investigate how lipids redistribute according to curvature in single- and two-component lipid bilayer simulations using the Cooke model for coarse-graining. In Paper II we also analyze lipid redistribution, but for Martini model simulations of one- to three-component lipid systems, with particular focus on the distribution of cardiolipin, a lipid with a unique structure which makes it a relatively strong curvature sensor. We also study how curvature affects membrane lipid structure, in terms of lipid order parameters. Table 6.1 summarizes the simulated systems reported in this chapter.

All lipid distributions depicted here correspond to the spatial distributions of the innermost lipid tail beads. Both leaflets are symmetric and equivalent: the curvature at some point in the upper monolayer is the same in magnitude, but of opposing sign at the same point the lower monolayer. Equivalently, the curvature at  $s_0$  in one monolayer, is the same as in  $s_0 + 0.5$  in the other, and  $K(s) = -K(s + 0.5)$ . Reported monolayer densities take the perspective of the upper monolayer.<sup>1</sup> These densities are constructed by taking directly the  $s$ -positions from lipids in the upper monolayer, and the  $s$ -positions of lipids in the lower monolayer shifted by a half period.

### 6.1 Geometric effects of curvature on lipid packing

In bilayers composed by a single lipid species, curvature sensing is absent, as the lipid positions are constrained to form continuous mono-

<sup>1</sup>Figure 6.1 shows, however, distributions for each monolayer separately.

**Table 6.1: Molecular dynamics simulations presented in this chapter.** The systems are listed by lipid composition, ion concentrations, buckling factors and simulation times. For the Cooke model lipC denotes cylindrical lipids, lipS and lipB denote small and big headed lipids with the head size ratio given in parenthesis (e.g., (0.9:1.1) denotes small headed lipids with parameter  $b_{\text{head}} = 0.9\sigma$  and big headed lipids with  $b_{\text{head}} = 1.1\sigma$ , while keeping the tail bead size constant, with  $b_{\text{tail}} = \sigma$ ). For the Martini simulations, the reported times are actual simulation times (i.e., no speed-up factors have been applied)

	CG Model	Lip. Composition	Ions	$\gamma$	Sim. time
CC0.2	Cooke	1024 lipC	-	0.2	$10^7\tau$
CC0.3	Cooke	1024 lipC	-	0.3	$10^7\tau$
CC0.4	Cooke	1024 lipC	-	0.4	$10^7\tau$
CC0.5	Cooke	1024 lipC	-	0.5	$10^7\tau$
CD1.05	Cooke	512 lipS, 512 lipB (0.95:1.05)	-	0.3	$6 \times 10^6\tau$
CD1.05b	Cooke	512 lipS, 512 lipB (0.95:1.05)	-	0.5	$6 \times 10^6\tau$
CD1.1	Cooke	512 lipS, 512 lipB (0.9:1.1)	-	0.3	$6 \times 10^6\tau$
allPG	Martini	512 PG	512 Na <sup>+</sup>	0.3	20 $\mu\text{s}$
allPE	Martini	512 PE	-	0.3	20 $\mu\text{s}$
CL0	Martini	128 PG, 384 PE	128 Na <sup>+</sup>	0.3	30 $\mu\text{s}$
CL4	Martini	120 PG, 384 PE, 8 CL	128 Na <sup>+</sup>	0.3	30 $\mu\text{s}$
CL12	Martini	104 PG, 384 PE, 24 CL	128 Na <sup>+</sup>	0.3	30 $\mu\text{s}$
CL12s	Martini	104 PG, 384 PE, 24 CL	335 Na <sup>+</sup> , 207 Cl <sup>-</sup>	0.3	30 $\mu\text{s}$
CL12b	Martini	104 PG, 384 PE, 24 CL	128 Na <sup>+</sup>	0.4	30 $\mu\text{s}$

layers. Simulation of single-component bilayers however is important as it allows us to study how the lipids redistribute due to membrane bending, to establish a standard for data sampling, and to evaluate the methodology, as done in Chapter 5, as well as to compute certain membrane properties, like lipid diffusion constants and autocorrelation times.

These observations are also applicable to multi-component lipid bilayers, when all lipids are taken together irrespective of lipid species. The lipid distributions show the geometric effects of membrane bending on lipid tail positions. When a bilayer is bent towards the lower monolayer, lipid head groups in the upper monolayer acquire increased available area, while the opposite is true for the innermost region of their tails. This is reflected in the single-component position distributions, as well as the distributions for all lipids taken together in multi-component distributions. As the simulated buckles contain fairly large curvatures, this effect is large and of order  $\gamma$  (Figs. 6.1 and 6.2).

Figure 6.1 shows the probability densities  $\rho(s)$  for each monolayer, and the midplane density  $\hat{\rho}(s)$  (taking into account lipids from both monolayers). Figure 6.2 depicts the same data as Fig. 6.1, but as a function of curvature  $K(s)$ , and where we have combined the data of both monolayers, by shifting the  $s$ -values of the lower monolayer by a half period:

$$\rho(s) = \frac{1}{2} \left[ \rho_{\text{upper}}(s) + \rho_{\text{lower}}(\text{mod}(s + 0.5, 1)) \right]. \quad (6.1)$$

For all the simulated systems with varying  $\gamma$ , the density is to excellent approximation a function of curvature only. The simplest geometric model is linear in curvature:

$$\rho(s) = \rho_0 + \alpha_1 K(s). \quad (6.2)$$

As Fig. 6.2a shows, this linear model is an excellent approximation. However, higher order deviations, though small can be observed. Although the linear model implies that the upper and lower monolayer densities balance out, it can be seen that the midplane density, though well approximated by  $\hat{\rho}(s) = 1$ , contains systematic deviations. This density is maximal where the bilayer is flat ( $K(s) = 0$ ), since lipid packing is best in those regions, and minimal around  $|K| 0.2\sigma^{-1}$ .

Similar observations are applicable for the Martini systems, where the densities  $\rho(s)$  are also well described by Eq. (6.2) (Fig. 6.3b), for the single-component bilayers as well as for the multi-component ones,

where  $\rho(s)$  is the all-lipid density. For these systems, however, the asymmetries in curvature-dependent lipid distribution are stronger. As shown in Fig. 6.3a,b, the depletion at minimal curvature is larger than the enrichment at the largest curvature region, while the profile of  $\rho(s)$  present a plateau around maximal  $K$ . The midplane density also deviates weakly from a flat density  $\hat{\rho}(s) = 1$  (Fig. 6.3c), showing maximal density at flat regions ( $s = \{0.25, 0.75\}$ ), where the tightest lipid packing occurs.

## 6.2 Curvature-dependent lipid distribution and structure

In multi-component bilayers, we can study how different lipid species redistribute due to curvature. The appropriate observables are the lipid distributions relative to the all-lipid density  $\rho(s)$  which was the subject of Section 6.1. Relative densities are defined as

$$\phi_j(s) = \frac{\rho_j(s)}{\sum_k \rho_k(s)} = \frac{\rho_j(s)}{\rho(s)}, \quad (6.3)$$

where  $\rho_j(s)$  is the monolayer distribution for lipid species  $j$ , normalized as

$$\int_0^1 ds \rho_j(s) = f_j, \quad (6.4)$$

where  $f_j$  is the fraction of that lipid in the monolayer, while  $\rho(s)$  is normalized to unity. For clarity, in Fig. 6.4, the depicted relative densities are normalized as

$$\Phi_j(s) = \frac{\phi_j(s)}{\int_0^1 ds \phi_j(s)}. \quad (6.5)$$

In Fig. 6.4 we observe how different lipids sense curvature with varying strengths. In the two-component bilayer, POPG redistributes towards positive curvature, while POPE is enriched in negative curvature regions. As CL is added to the mixture in increasing concentrations, it shows a stronger preference for negative curvature, outcompeting POPE for the largest negative curvature region, partially displacing POPE.

To investigate how curvature affects lipid structure, we calculate the second rank order parameter

$$P_2(s) = \frac{1}{2}(3\langle \cos^2 \theta \rangle - 1), \quad (6.6)$$

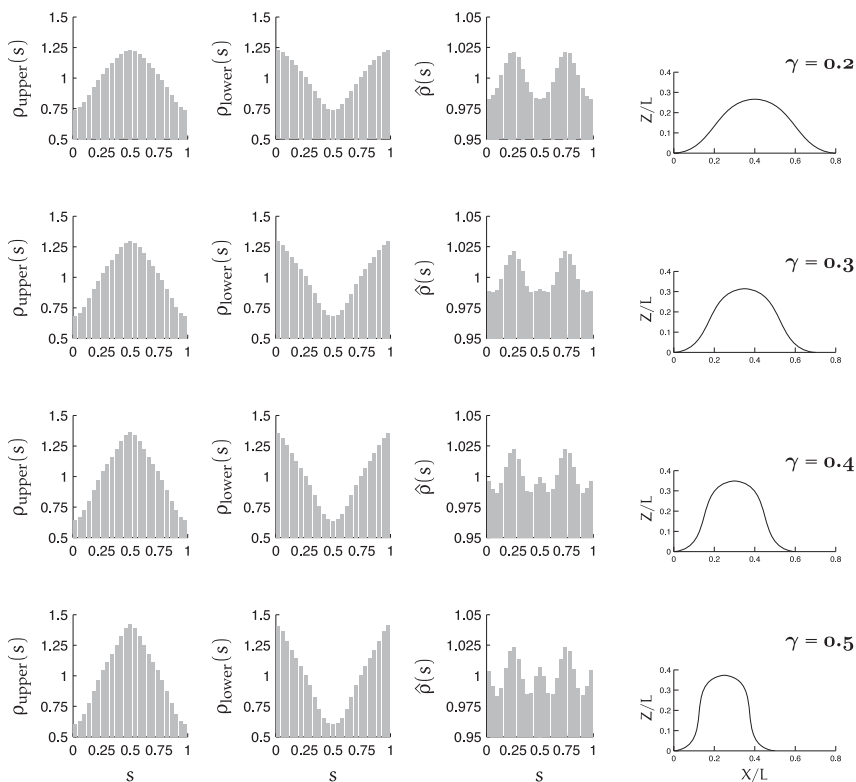


**Figure 6.1:** Probability densities for lipid position for different values of  $\gamma$  for the Cooke systems. The first column corresponds to the lipids in the upper leaflet, the second column to the lower leaflet, and the third column to both leaflets. The fourth column corresponds to the fitted theoretical buckled shape, in units of the bilayer arc length  $L$ . The analyzed data includes the positions of all lipid tails. Simulation time is  $10^7 \tau$ . Adapted with permission from Paper I. © 2018 ACS.

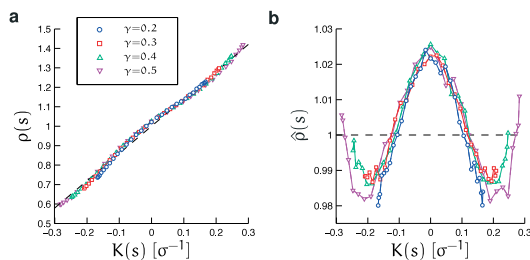


**Figure 6.2:** (a) Monolayer lipid densities as functions of curvature for different values of  $\gamma$ , for the Cooke simulations (Table 6.1). Same data as in the first two columns of Fig. 6.1, but plotted as function of  $K(s)$ . The dashed line is the linear model Eq. (6.2), with  $\rho_0 = 1$  (a flat monolayer) and  $\alpha_1 = 1.42 \sigma$ , obtained from a least-squares fit. (b) Midplane density  $\hat{\rho}(s)$  corresponding to the third column in Fig. 6.1. Adapted with permission from Paper I. © 2018 ACS.

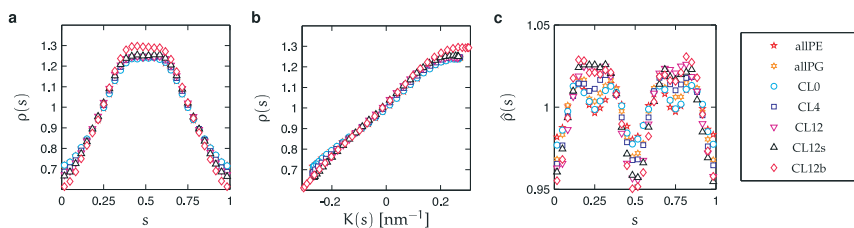


**Figure 6.3:** Monolayer density  $\rho(s)$  for all lipids, as function of  $s$  (a) and of curvature  $K(s)$  (b), and midplane density  $\hat{\rho}(s)$  (c), for the Martini simulations listed in Table 6.1. Adapted from Paper II.

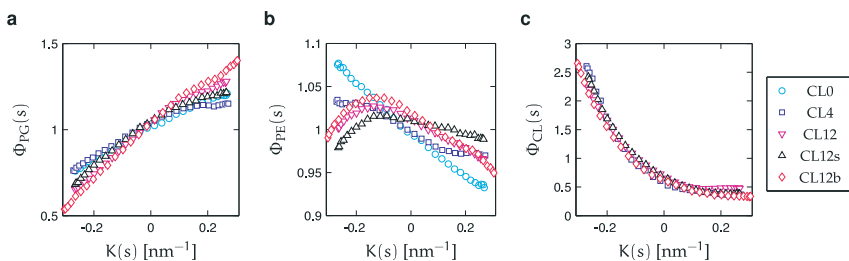


**Figure 6.4:** Normalized relative densities  $\Phi_j(s)$  as functions of curvature  $K(s)$  for the Martini simulations. Panels correspond to (a) POPG, (b) POPE, and (c) CL. Symbols correspond to the simulated systems listed in Table 6.1. Adapted from Paper II.

for the lipid tails as a function of local curvature. Here  $\theta$  is the angle between a lipid tail bond and the bilayer normal at the location of the lipid. For each bond, the average is done over all lipids within the same bin in  $s$ . Figure 6.5 shows the order parameter  $\langle P_2 \rangle$ , averaged over all the tail bonds for each lipid species, as functions of curvature  $K(s)$ . The order parameters for POPG and POPE are very similar. This is expected since the tail compositions for these two lipids are identical, only varying in their head groups. For all the multi-component simulations, the  $P_2$ -values for POPG are slightly larger, likely due to the fact that the charged head group in POPG keeps the molecules a little more elongated. As expected, in all cases  $P_2$  is maximal at flat regions,  $K \sim 0$ , and is minimal at the most negative curvature region. CL molecules are the most affected by curvature in terms of  $P_2$ , consistent with the picture of CL preferring negative curvature regions, where there is increased available area for the lipid tails to spread, making it entropically favourable. This mechanism is similar to the role of cholesterol, filling the gaps left in fluid bilayers with many unsaturated lipids [85], and is also consistent with CL function to stabilize protein-lipid domains, by filling the gaps in the protein-membrane interface [86].

### 6.3 Theoretical analysis of lipid sorting for two- and three-component bilayers

Here we provide a derivation of the so-called enhancement ratio [39], a quantity that measures lipid partitioning between regions of positive and negative curvature, for two- and three-component lipid mixtures.

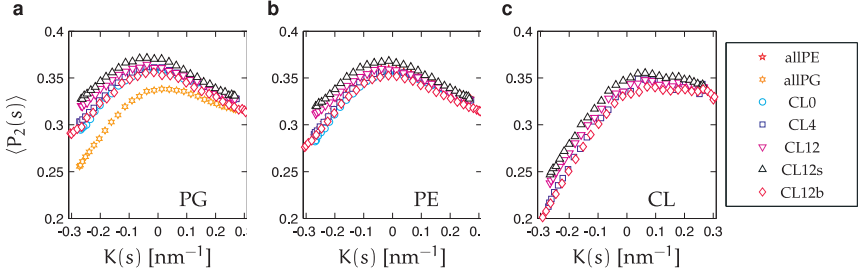


**Figure 6.5:** Average order parameter  $\langle P_2 \rangle$  as a function of curvature  $K(s)$ . Panels correspond to (a) POPG, (b) POPE, and (c) CL. Symbols correspond to the simulated systems listed in Table 6.1. Adapted from Paper II.

Following Ref. [39], we model the curvature energy per lipid of species  $j$  as

$$E_j = \frac{1}{2} M_j (K(s) - K_j)^2, \quad (6.7)$$

where  $M_j$  is the bending modulus, and  $K_j$  the lipid's intrinsic curvature. Mixing entropy per lipid in the monolayer is given by the ideal gas relation

$$S = -k_B (\log \phi_j(s) - 1), \quad (6.8)$$

where  $\phi_j(s)$  is the local mole fraction for lipid species  $j$  defined in Eq. (6.3).

Consider a three-component lipid mixture. From Eqs. (6.7,6.8), the free energy per monolayer is given by

$$F = L_y L \int_0^1 ds \tilde{\rho}(s) \sum_{j=1}^3 \left( \frac{\phi_j(s)}{2} M_j (K(s) - K_j)^2 + k_B T \phi_j(s) (\log \phi_j(s) - 1) \right), \quad (6.9)$$

where  $\tilde{\rho}(s) = n\rho(s)$  is the lipid number density, with  $n$  being the total number of lipids in the monolayer. Equation (6.9) is subject to the constraints

$$\int_0^1 ds \tilde{\rho}(s) \phi_j(s) = n_j, \quad (6.10)$$

which fixes the number  $n_j$  of lipids of species  $j$  in the monolayer, and

$$\sum_{i=1}^3 \phi_i(s) = 1, \quad (6.11)$$

which ensures point-wise normalization of the molar fractions. Minimizing Eq. (6.9) with respect to  $\phi_i(s)$  yields

$$-k_B T \log \phi_j(s) = \frac{M_j}{2} (K(s) - K_j)^2 + \mu_j + \alpha(s). \quad (6.12)$$

Here  $\mu_j$  is a Lagrange multiplier, corresponding to a chemical potential, that arises from condition (6.10), and  $\alpha(s)$  is a function which enforces the point-wise constraint (6.11). For the function  $\alpha(s)$  we find

$$e^{\alpha(s)} = \sum_{j=0}^3 e^{-\mu_j - \frac{M_j}{2} (K(s) - K_j)^2}. \quad (6.13)$$

The curvature at any given point  $s$  in opposing monolayers has the same magnitude and opposing sign ( $K_{\text{upper}}(s) = -K_{\text{lower}}(s)$ ). Thus, from Eq. (6.12), and taking both monolayers into account leads to the expression

$$\log \frac{\phi_j^+(s)}{\phi_j^-(s)} = \frac{2}{k_B T} K(s) (K_j M_j) + \mu_j^+ - \mu_j^- - (\alpha^+(s) - \alpha^-(s)), \quad (6.14)$$

where  $\phi_j^+(s)$  is the mole fraction of lipid species  $j$  at point  $s$  in the leaflet with positive curvature, and conversely  $\phi_j^-(s)$  is the same quantity at the leaflet with negative curvature. The same notation applies for  $\mu^\pm$  and  $\alpha^\pm$ . Since the monolayers are symmetric the chemical potentials are the same. The function  $\alpha(s)$  on the other hand is not symmetric across the bilayer. Fortunately, however, it cancels out for expressions of relative fractions ( $\log(\phi_i/\phi_j)$ ). Incorporating these considerations, we arrive at the enhancement ratio equation for a three-component mixture

$$\log \frac{\phi_i^+(s) \phi_j^-(s)}{\phi_i^-(s) \phi_j^+(s)} = 2K(s) \frac{K_i M_i - K_j M_j}{k_B T}. \quad (6.15)$$

For a two-component bilayer, if one assumes  $K_j M_j = 0$ , it follows that

$$\log \frac{\phi^+(s)}{\phi^-(s)} = 2K(s) \frac{K_i M_i}{k_B T}, \quad (6.16)$$

which was derived in Ref. [39], where the quantity on the left hand side is referred to as the enhancement ratio, and measures the degree of partitioning, through lipid flip-flop, of big-headed Cooke lipids between the outer monolayer (corresponding to positive curvature) and

the inner monolayer (which has negative curvature) in vesicles of varying sizes.

Analogously to [39], we simulated buckled membranes with 1:1 mixtures of small-headed and big-headed Cooke lipids, varying the degree of buckling, and the head size ratio, which is achieved by varying the parameter  $b$  in the potential (4.2). These simulations are listed as CD1.05, CD1.05b and CD1.1 in Table 6.1, where the simulation parameters are reported. In Fig. 6.6 we compare the results of these simulations, to those obtained in [39] with simulated vesicles. We find excellent agreement, except for the two highest curvature points, which we suspect may be outliers. The results are in agreement with Eq. (6.16), which predicts a linear relation between the enhancement ratio and local curvature, and that the slope of the line depends only on the material constants  $K_i$  and  $M_i$ , and not the particular geometry of the membrane. Here, a particular advantage of the simulated buckling is that a continuous range of curvature can be investigated in a single simulation, in contrast to the assay in [39], where each data point corresponds to a distinct simulated vesicle.

For the two- and three-component Martini simulations, Fig. 6.7 shows weak competition between POPG and POPE ( $K_{PG}M_{PG} - K_{PG}M_{PG} \approx 1.2k_B Tn m$ ), strong competition between POPG and CL, since the lipids redistribute to curvatures of opposing signs ( $K_{PG}M_{PG} - K_{CL}M_{CL} \approx 4.6k_B Tn m$ ), and intermediate competition between POPE and CL ( $K_{PE}M_{PE} - K_{PG}M_{PG} \approx 3.4k_B Tn m$ ), consistent with our previous results indicating that CL outcompetes POPE for negative curvature. Equation (6.15) predicts a linear relation between curvature and the enhancement ratios for each pair of lipids, which moreover should be the same for all mixtures. Figure 6.7 shows good agreement between our simulations and Eq. (6.15).

In Ref. [87], a similar system of a buckled bilayer containing a mixture of POPC, POPE and CL was studied. Our results are in agreement to their findings that CL strongly prefers negative curvature, in contrast to POPE which, though having a similar inverted conical shape, appears to be fairly curvature agnostic. Their parameterization of the buckled membrane consists of fitting local curvature in terms of the buckling axis coordinate ( $x$  in our nomenclature), thus assigning a curvature value to each lipid based on the  $x$  coordinate of the lipid's head bead. This allows for the study of lipid species concentration gradients as functions of curvature, but lacking a position coordinate relative to

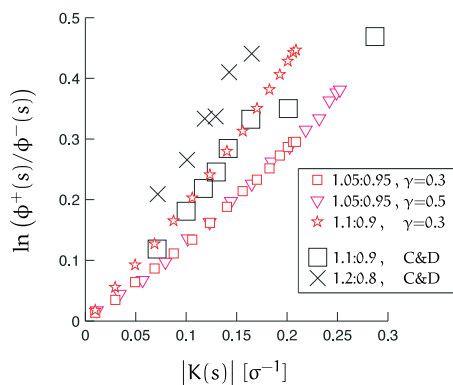


**Figure 6.6:** Enhancement ratio as function of absolute total curvature  $|K|$  (twice the mean curvature), for different head-size ratios. The colored symbols correspond to the CD1.05, CD1.05b and the CD1.1 simulations (see Table 6.1). The data marked C&D in the legend was taken from Fig. 4 in Ref. [39]. Reprinted with permission from Paper I. © 2018 ACS.

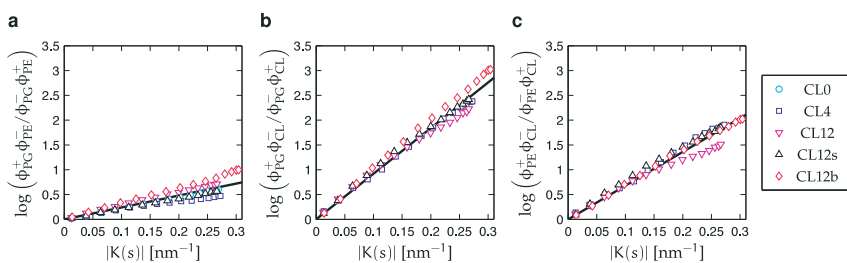


**Figure 6.7:** Enhancement ratios for the two- and three-component Martini simulations, as functions of total curvature  $|K|$ . The black lines are least-squares fits to Eq. (6.15). Adapted from Paper II.

the buckle ( $s$ ), the parameterization is not amenable to the kind of analysis presented in this section.



# 7. Curvature sensing by proteins and peptides (I,III,IV)

In this chapter we investigate curvature sensing by peptides and proteins. We start with a short overview of the theory for direction-dependent curvature sensing, and make an argument for the need of quadratic models in the curvature tensor. We then proceed to study three kinds of simulated types of curvature sensing assays, with peptides and proteins acting as curvature sensors. First, we constructed a system consisting of a model trimeric transmembrane protein in a buckled membrane employing the Cooke model for Coarse-graining, where we studied the curvature preferences of the trimer both in terms of its position along the buckle, and its orientation within the buckle (Paper I). Second, we simulated three Martini systems, each containing a small amphipathic peptide bound to the surface of a buckled membranes (Paper III). Third, using again the Cooke model, we simulated a series of model multimeric transmembrane proteins, with 1- to 6-fold rotational symmetry, attached to a cylindrical membranes (Paper IV). The principal curvatures in cylinders are zero in the longitudinal direction, and  $1/R$  in the circumferencial direction, thus the local curvature of the proteins is a function only their orientation angle. Table 7.1 summarizes the simulations reported in this chapter.

## 7.1 Position- and orientation-dependent curvature sensing

We model the position distribution of a curvature sensing probe as depending on local curvature,  $G = G(K(s))$ , where  $G$  is the orientation averaged binding free energy in units of  $k_B T$ . The distribution is proportional to the Boltzmann factor  $\exp(-G(s))$ , so we calculate the free energy  $G$  from curvature histograms by weighting the bins by its trans-

**Table 7.1: Molecular dynamics simulations presented in this chapter.** The systems are described by the coarse-graining model used, the kind of curvature sensing probe, the topology of the membrane including the compression factor  $\gamma$  for buckled membranes, or the radius for the cylinders (here lipC denotes cylindrical Cooke lipids), the number of replicas and total simulation time, including all replicas (in the cylinder simulations, some replicas were run for  $10^6\tau$ , while others for  $2 \times 10^6\tau$ ). Martini simulations were solvated with  $\sim 21,000$  CG polarizable water molecules, and  $\text{NA}^+$  CG ions ( $\sim 300$ ) were added to neutralize the systems. Cooke simulations are solvent-free and all molecules electrically neutral. Reported times are actual simulation times (i.e., no speed-up factors have been applied)

	CG Model	Probe	Membrane topology	Replicas	Sim. time
C3 $\gamma$	Cooke	Trimer	5966 lipC, $\gamma = 0.2$	1000	$10^9\tau$
MAG	Martini	Magainin	308 POPG, 716 POPE, $\gamma = 0.2$	3	60 $\mu\text{s}$
MEL	Martini	Melittin	308 POPG, 716 POPE, $\gamma = 0.2$	3	60 $\mu\text{s}$
LL-37	Martini	LL-37	308 POPG, 716 POPE, $\gamma = 0.2$	3	60 $\mu\text{s}$
C1R07	Cooke	Monomer	4550 lipC, $R = 7\sigma$	35	$6 \times 10^7\tau$
C1R10	Cooke	Monomer	6520 lipC, $R = 10\sigma$	30	$5 \times 10^7\tau$
C1R15	Cooke	Monomer	12290 lipC, $R = 15\sigma$	100	$1.1 \times 10^8\tau$
C1R20	Cooke	Monomer	16420 lipC, $R = 20\sigma$	100	$1.25 \times 10^8\tau$
C1R25	Cooke	Monomer	20480 lipC, $R = 25\sigma$	100	$1.25 \times 10^8\tau$
C1R33	Cooke	Monomer	27060 lipC, $R = 33\sigma$	100	$1.7 \times 10^8\tau$
C1R50	Cooke	Monomer	41060 lipC, $R = 50\sigma$	26	$2.7 \times 10^7\tau$
C2R20	Cooke	Dimer	16390 lipC, $R = 20\sigma$	25	$2.5 \times 10^7\tau$
C3R07	Cooke	Trimer	4520 lipC, $R = 7\sigma$	50	$5 \times 10^7\tau$
C3R20	Cooke	Trimer	16370 lipC, $R = 20\sigma$	50	$5 \times 10^7\tau$
C4R10	Cooke	Tetramer	6460 lipC, $R = 10\sigma$	50	$1 \times 10^8\tau$
C4R15	Cooke	Tetramer	12230 lipC, $R = 15\sigma$	55	$1.1 \times 10^8\tau$
C4R20	Cooke	Tetramer	16350 lipC, $R = 20\sigma$	55	$1.1 \times 10^8\tau$
C4R25	Cooke	Tetramer	20420 lipC, $R = 25\sigma$	55	$1.1 \times 10^8\tau$
C4R33	Cooke	Tetramer	26990 lipC, $R = 33\sigma$	65	$1.3 \times 10^8\tau$
C4R50	Cooke	Tetramer	41000 lipC, $R = 50\sigma$	32	$3.2 \times 10^7\tau$
C5R20	Cooke	Pentamer	16340 lipC, $R = 20\sigma$	25	$5 \times 10^7\tau$
G6R20	Cooke	Hexamer	16330 lipC, $R = 20\sigma$	25	$5 \times 10^7\tau$

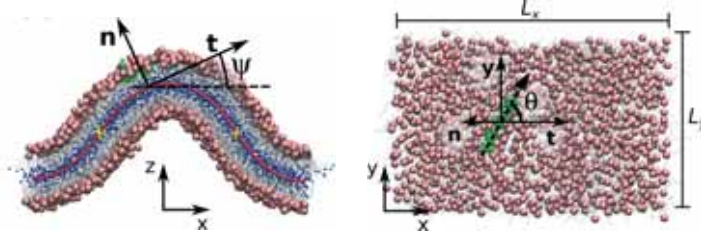


**Figure 7.1:** Side and top views of a simulated buckled membrane with a bonded peptide (green). The red curve is the fitted theoretical buckled shape. The position of the peptide correspond to the projection of it's center of mass to the red curve, in terms of the normalized arc length  $s$ . Lipid phosphate groups are marked in pink, lipid tails in gray, and the innermost tail beads in blue. The orientation angle  $\theta$  is defined as the angle between the local tangent angle  $t$  and the projection of the peptide's backbone to the local tangent plane. These snapshots correspond to the LL-37 simulation. Adapted from Paper III.

formation Jacobian factor  $|dK/ds|$

$$\tilde{\rho}(s)ds \propto e^{-G(K(s))} ds \propto e^{-G(K)} \left| \frac{dK}{ds} \right|^{-1} dK \propto \rho(K)dK. \quad (7.1)$$

The Jacobian factor can be understood as compensating for the fact that, in a buckled shape, near flat curvatures have short arc length footprints while larger curvature bins correspond to longer ranges in  $s$ . Thus, the curvature dependent free energy is given by

$$G(K) = -\log \left( \rho(K) \left| \frac{dK}{ds} \right| \right) + \text{const}. \quad (7.2)$$

Alternatively, the same curve can be obtained by plotting  $G(s)$  as a function of  $K(s)$ , though the data points in the  $x$ -axis will be unevenly spaced (Fig. 7.3d).

A common approach to modeling direction-dependent curvature sensing is to take the binding energy as a function of the local curvature tensor seen from a coordinate system bound to the protein [88–91]. In a coordinate system rotated by  $\theta$  with respect to one of the principal curvature directions (Fig. 7.1), the local curvature tensor is given by

$$C_{ij} = \begin{pmatrix} C_{\parallel} & C_{\chi} \\ C_{\chi} & C_{\perp} \end{pmatrix} = \begin{pmatrix} H + D \cos 2\theta & D \sin 2\theta \\ D \sin 2\theta & H - D \cos 2\theta \end{pmatrix}, \quad (7.3)$$

where  $H = (c_1 + c_2)/2$  and  $D = (c_1 - c_2)/2$  are the mean and deviatoric curvatures, and  $c_1$  and  $c_2$  the principal curvatures. The total curvature is  $K = c_1 + c_2 = C_{\parallel} + C_{\perp}$ , and Gaussian curvature is given  $K_G = c_1 c_2 = C_{\parallel} C_{\perp} - C_X^2$ . For both the buckled shape, and the cylinders,  $c_2 = 0$ , hence  $K_G = 0$ , and  $H = D = K/2$ . In (7.3), the orientation angle  $\theta$  enters only in terms  $\cos 2\theta$  and  $\sin 2\theta$ . Thus, if the binding energy is a function only of  $C_{ij}$ , the Boltzmann distribution is invariant under 180-degree rotations,  $(s, \theta) \rightarrow (s, \theta + 180)$ .

A general linear model in  $C_{ij}$  can be written as  $E_1 = aH + bD \cos(2(\theta - \alpha))$  [88]. Integrating out the angular dependence, and setting  $H = D = K/2$  yields

$$G_1 = -\log \int_0^{2\pi} d\theta e^{-E_1} = aK/2 - \log I_0(bK/2) + \text{const.} \quad (7.4)$$

The modified Bessel function  $I_0$  is convex. Therefore  $G_1$  is concave, for  $b \neq 0$ , or linear as  $b \rightarrow 0$ . This argument rules out linear models, as the functions  $G(K)$ , for the systems presented here are convex (Figs. 7.3 and 7.6).

A general quadratic model takes the form

$$E_2 = a_1(C_{\parallel} - a_2)^2 + a_3(C_X - a_4)^2 + a_5(C_{\perp} - a_6)^2 + a_7 C_{\parallel} C_{\perp} + a_8 C_{\parallel} C_X + a_9 C_{\perp} C_X. \quad (7.5)$$

For our systems, this model is however unidentifiable, since the Gaussian curvature  $K_G = 0$ . Based on a quadratic models studied in [89, 90, 92, 93], we propose a simplified quadratic model with curvature sensing along the longitudinal and transverse directions only, and incorporating the observation that the curvature sensing direction may not be necessarily aligned with the peptide backbone's used to define the probe orientation (Fig. 7.4):

$$E_C = \frac{\kappa}{2}(2H - K_0)^2 + bD \cos(2(\theta - \alpha)) + \kappa_G K_G. \quad (7.6)$$

The coefficient  $\kappa_G$  is unidentifiable since  $K_G = 0$ . Since Gaussian curvature is rotationally invariant, this terms affects overall preference to membranes with Gaussian curvature but does not affect orientational preferences. Integrating out the orientation angle  $\theta$ , and again setting  $H = D = K/2$  yields

$$G_C = -\log \int_0^{2\pi} d\theta e^{-E_C} = \frac{\kappa}{2}(K - K_0)^2 - \log I_0(bK/2). \quad (7.7)$$

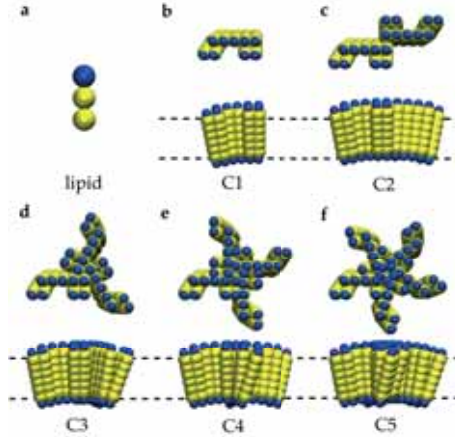


**Figure 7.2:** Side and top view of (b) the asymmetric monomer (C1); and (c-f) the dimer (C2), trimer (C3), tetramer (C4), and pentamer (C5), which are formed with rotated copies of the monomer. Panel (a) shows a single Cooke lipid. All the structures are constructed using these Cooke lipid beads. Adapted from Paper IV.

An important observation is that the model predicts the presence of a preferred curvature  $K_0$ .

## 7.2 Trimer in a buckled membrane (Paper I)

We constructed a model trimeric protein consisting of three copies of an asymmetric monomer. This monomer is formed by 54 Cooke tail beads, sandwiched between two layers of 9 Cooke head beads each. The monomers have a wedge-like shape with curvature radii of  $5\sigma$  in the transverse direction, and  $25\sigma$  in the longitudinal direction (Fig. 7.2b). Given this shape, we expect that the monomer and the trimer to show a preference for curved membranes. Three rotated monomers are placed together to form a trimer with three-fold rotational symmetry (Fig. 7.2d). The structure is stabilized by an elastic network of harmonic bonds with strength  $100\epsilon/\sigma^2$  between all bead pairs within a distance  $4\sigma$ .

We simulated a buckled membrane consisting of 5966 Cooke lipids and one copy of the trimer just described, acting as the curvature sensing probe, listed as **C3 $\gamma$**  in Table 7.1. We used custom Matlab scripts to construct a flat bilayer, insert the transmembrane trimeric proteins,

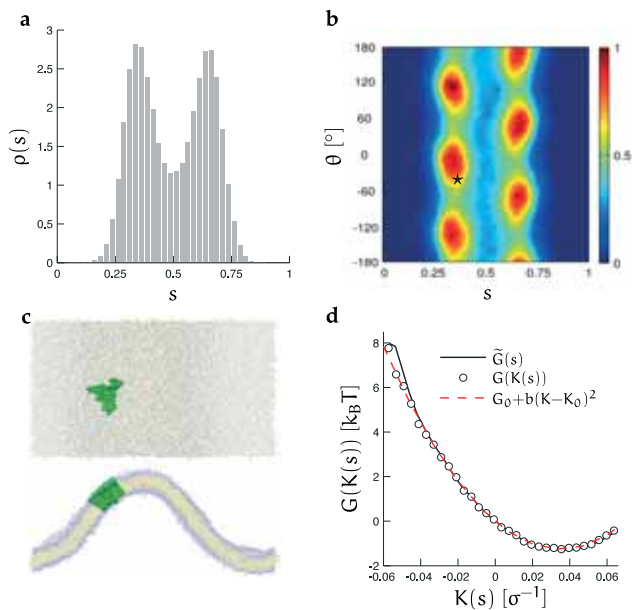
and remove overlapping lipids. The membrane was then energy minimized and equilibrated with pressure coupling in the  $x$ -direction. Then, the membrane was compressed with factor  $\gamma = 0.2$  along the  $x$ -axis, again energy minimized and equilibrated for  $10^5 \tau$  at constant volume. We ran one thousand replicas, with different initial positions, each for  $10^6 \tau$ . The initial  $5 \times 10^5 \tau$  in each replica were discarded as equilibration (based on the trimers autocorrelation time, see Appendix A).

Figure 7.3 depicts the results from the **C3 $\gamma$**  system. The position distribution depicted in Fig. 7.3a shows that the trimer prefers intermediate curvature. From the quadratic fit in Fig. 7.3d, the estimated preferred curvature is  $K_0 = 0.035\sigma^{-1}$ . This observation is remarkable in the sense that the existence of a preferred curvature is predicted by standard quadratic theoretical models, but it has shown elusive in most curvature sensing assays, where curvature sensors typically localize to the maximal curvature available [2–4, 45]. Recently, a couple of exceptions were presented in [5, 6].

The joint position-orientation distribution  $\rho(s, \theta)$  of the trimer is shown in Fig. 7.3b. The structural symmetry of the trimer implies that  $\rho(s, \theta)$  is invariant under  $\pm 120^\circ$  rotations,  $(s, \theta) \rightarrow (1 - s, \theta + 120^\circ)$ . The distribution is also symmetric to rotations of  $180^\circ$  to the entire system around the  $z$ -axis,  $(s, \theta) \rightarrow (1 - s, \theta + 180^\circ)$ . Both this symmetries are observed in Fig. 7.3b. Equation (7.3) implies an additional symmetry of  $180^\circ$  rotations to the trimer,  $(s, \theta) \rightarrow (s, \theta + 180)$ . The symmetry is however not present in Fig. 7.3b, likely due to the fact that the local curvatures at which individual monomers are located are slightly different, thus the trimer effectively senses a curvature gradient, which is not invariant under  $180^\circ$  rotations.

### 7.3 Amphipathic helices in a buckled membrane (Paper III)

In this section we investigate the curvature sensing properties of three amphipathic antimicrobial peptides: magainin [94], melittin [95], and LL-37 [96]. Their structures are shown in Fig. 7.4. We simulated three systems using Martini for coarse graining. Each system is composed of a buckled membrane containing 1024 lipids of which 70% are POPE, and 30% POPG, one of the peptides, solvated with around 21,000 polarizable water CG beads, and neutralized with  $\text{Na}^+$  CG beads (Table 7.1).



**Figure 7.3:** (a) Normalized distribution of the arc length position  $s$  from the trimer simulation. (b) Joint distribution  $\rho(s, \theta)$  of the position and orientation of the trimer. Density is indicated by colors from blue (low probability) to red (high probability). (c) Trajectory snapshots from top and side perspectives, the  $s$  and  $\theta$  values correspond to the star in panel b. (d) Free energy  $G(K(s))$  versus curvature, where  $G(K(s))$  is given in Eq. (7.2), and  $\tilde{G}(s) = -\log(\tilde{\rho}(s))$ . The red dashed line is a quadratic least-squares fit to the data shown in circles, with fitted parameters  $K_0 = 0.035 \sigma^{-1}$ ,  $b = 1005 k_B T \sigma^2$ , and  $G_0 = -1.26 k_B T$ . Reprinted with permission from Paper I. © 2018 ACS.

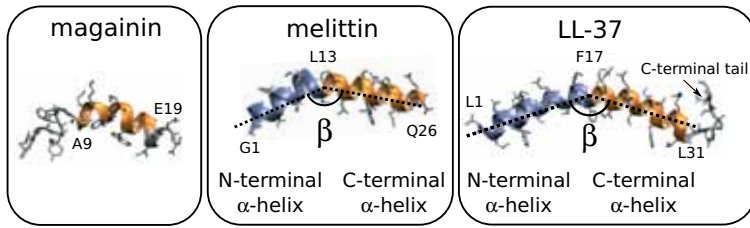


**Figure 7.4:** Structures of the amphipathic peptides magainin, melittin and LL-37. Shown in orange are C-terminal  $\alpha$ -helices, and in blue N-terminal  $\alpha$ -helices, with labels indicating the limiting amino acids. Shown in grey are side-chains and non helical residues. Melittin and LL-37 contain two  $\alpha$ -helices, forming angles marked  $\beta$ . Adapted from Paper III.

First, flat bilayers were assembled, energy minimized, and equilibrated for 25 ns. Then the bilayers were compressed with factor  $\gamma = 0.2$ , and again minimized and equilibrated for another 25 ns. Then, a peptide molecule was placed about 3 nm above the membrane, which quickly attached to the bilayer surface. Finally we started production runs of 20  $\mu$ s, of which the first 5  $\mu$ s were discarded as equilibration. Three independent replicas were run for each of the three peptides.

All the peptides show a preference for positive curvature, localizing to the region around maximum curvature at  $s = 0.5$  (Figs. 7.5 and 7.7b). This is consistent with the cylindrical hydrophobic insertion mechanism. In the case of LL-37, the peptide localizes slightly off  $s = 0.5$ . This is likely due to the actual curvature sensing site not coinciding with the center of mass of the protein, used to define its  $s$ -position.

The orientation angle distributions (Figs. 7.5 and 7.7a) are however different for each of the peptides. Magainin shows very weak orientational preference, likely because its  $\alpha$ -helix is very short, and creates a near-symmetric insertion footprint. The angle  $\beta$  between the N-terminal and the C-terminal helices of melittin is broadly distributed, yet both helices show a preferred orientation towards  $\theta_{\max} \approx -15^\circ, 165^\circ$ , close to parallel to the  $x$ -direction. LL-37 maintains a linear structure ( $\beta \approx 180^\circ$ ), and shows preferred orientation at  $\theta_{\max} \approx 70^\circ, -110^\circ$ . In disagreement with the prediction of cylindrical hydrophobic insertion mechanism [97], none of the peptides aligns with the flat direction  $\theta = 90^\circ$ . Also absent is the mirror symmetry ( $\theta \rightarrow -\theta$ ) predicted by cylindrical shaped inclusions. The symmetry is broken by the handedness of the helices, and by the sequences of the peptides, indicating that

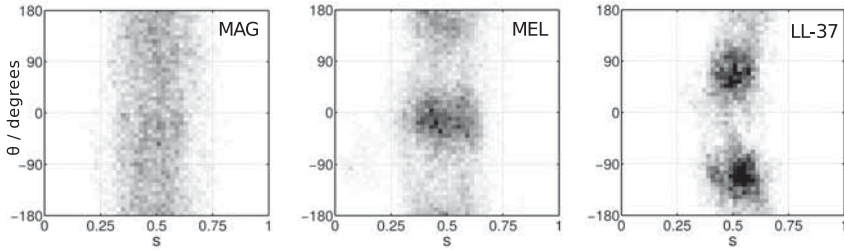


**Figure 7.5:** Joint distributions for the orientation angle  $\theta$  and position  $s$  in the buckled bilayer for magainin, melittin (the angle corresponds to that of the C-terminal) and LL-37. Adapted from Paper III.

there is more to the picture than shape-based effects. The  $E_C$  model, Eq. (7.6), successfully describes these distributions, as it does not assume that the curvature sensing directions are necessarily aligned to the peptides helices, but to be offset by the angle  $\alpha$ , leading to effective curvature sensing directions  $\theta^* = \theta - \alpha = 0, 90^\circ$ , which map unto themselves under reflection.

We fit the  $(s, \theta)$  distributions in Fig. 7.5 to Boltzmann distributions  $\exp(-E(s, \theta))/Z$ , for the  $E_C$  model, Eq. (7.6). The resulting fit parameters are given in Table 7.2. Figure 7.6 shows the orientation averaged free energy profiles  $G(K)$ , Eq. (7.2), for the three peptides. These are well described by quadratic fits. Fig. 7.6 also shows a comparison to the free energy for the  $E_C$  model, Eq. (7.7), using the fit parameters in Table 7.2. There is good agreement for magainin and melittin, but less so for LL-37. This is most likely a consequence of the effective curvature sensing site of LL-37, not coinciding with its center of mass. Figure 7.7 shows the marginal distributions of the angle  $\theta$  and of position  $s$ . The distributions are reasonably well described by the  $E_C$  model. The fits are not improved by using the full quadratic model  $E_2$ , Eq. (7.5).

## 7.4 Symmetric proteins in cylindrical bilayers (Paper IV)

Homo-oligomeric proteins are composed of a few, non-covalently bonded, identical protein chains. The majority of proteins found in living cells form symmetric oligomers [98]. For transmembrane proteins, the most common symmetry present corresponds to rotational symmetry around

**Table 7.2:  $E_C$ -fit parameters.** For each system, the listed values correspond to least-squares fits of the Boltzmann distributions  $\exp(-E_C(s, \theta))/Z$  to  $(s, \theta)$  histograms of the aggregated data from the three replicas, and bootstrap SD from 1000 realizations using blocks of 500 ns (100 data points) as the unit for resampling.

	$\kappa$ [ $k_B T \text{ nm}^2$ ]	$K_0^{-1}$ [ $\text{nm}$ ]	$b$ [ $k_B T \text{ nm}^2$ ]	$\alpha$ [ $^\circ$ ]
magainin	$72 \pm 26$	$3.4 \pm 0.7$	$-1.1 \pm 0.3$	$-40 \pm 8$
melittin	$150 \pm 50$	$4.3 \pm 0.5$	$-6.4 \pm 0.4$	$-16 \pm 2$
LL-37	$332 \pm 140$	$4.2 \pm 0.6$	$-8.9 \pm 0.6$	$69 \pm 2$

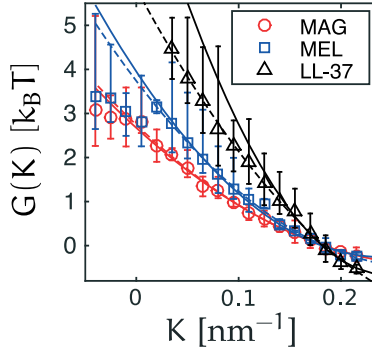


**Figure 7.6:** Orientation averaged binding free energy  $G(K)$ , Eq. (7.2), as function of local curvature  $K$  at the peptide's center of mass. The error bars correspond to the minimum and maximum values obtained from three independent simulations. Dashed lines are quadratic fits, and the solid lines are fits to the  $E_C$  model, using the fit parameters in Table 7.2. Adapted from Paper III.

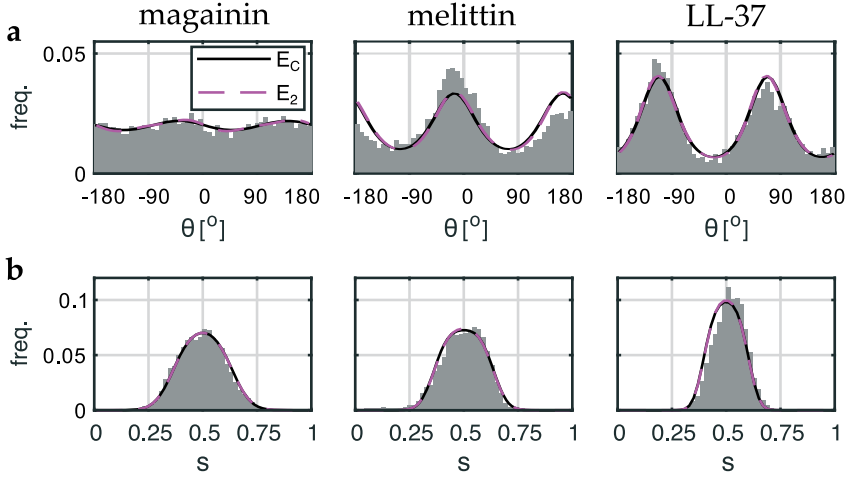


**Figure 7.7:** Marginal distributions of (a) the orientation angle  $\theta$ , and (b) the position  $s$ , for the three peptides. The curves correspond to least-square fits to the Boltzmann distributions  $\exp(-E(s, \theta))/Z$ . Solid line corresponds to the  $E_C$  model, Eq. (7.6), and dashed lines to the general quadratic model (with  $\alpha_9 = 0$ ), Eq. (7.5). The fitted parameters for the  $E_C$  model are given in Table 7.2. Adapted from Paper III.

the membrane normal. In this section, through coarse grained simulations, using the Cooke model, and theoretical arguments, we discuss how direction-dependent curvature sensing is easily observable for monomers, dimers and tetramers, but largely absent for odd and higher order symmetric multimers (unless curvatures are very high, as was the case for the trimer in Section 7.2).

Starting with the asymmetric monomer described in Section 7.2 and following the same procedure, we constructed a series of five multimers with 2- to 6-fold cyclic symmetry (Fig. 7.2). First, we simulated six systems, consisting of a cylindrical bilayer with radius  $R = 20\sigma$ , and height  $H = 75\sigma$ , and one of the multimers or the asymmetric monomer. Then, for the monomer and the tetramer systems, we varied the radius of the cylinder from  $R = 7\sigma$  to  $R = 33\sigma$ , running nine additional simulations. Finally, we also simulated a trimer in a cylinder with  $R = 7\sigma$ . For each system, multiple independent replicas were set up, and production runs of  $10^6\tau$  or  $2 \times 10^6\tau$  were simulated. Table 7.1 summarizes relevant simulation parameters. The remaining parameters, common to all the Cooke simulations, are listed in Section 4.1.1.

Cylindrical membranes present uniform curvature across the mem-

brane surface, therefore the curvature tensor associated with the curvature sensing protein, Eq. (7.3), depends only on the protein's in-plane orientation angle  $\theta$ . The protein position along the membrane surface is not relevant. Fig. 7.8 shows the  $\theta$  distributions of a single subunit for each of the different proteins. It also shows the corresponding free energy profiles, where we have enforced the structural rotation symmetry of the proteins (by taking the aggregated  $\theta$  value of all subunits), and the invariance to  $180^\circ$  rotations of the whole system, around an axis perpendicular to the axis of the cylinder. The monomer, dimer and tetramer show non-flat distributions, revealing their orientational preferences, while the trimer, pentamer and hexamer appear insensitive to orientation-dependent curvature.

To answer why this is the case, we model the binding free energy as a function of the local curvature tensor, Eq. (7.3),  $G = G(C_{ij})$ , and Taylor expand in terms of  $C_1 = (C_{\parallel} + C_{\perp})/2 = H$ ,  $C_2 = (C_{\parallel} - C_{\perp})/2 = D \cos(2\theta)$ , and  $C_3 = C_{\chi} = D \sin(2\theta)$ :

$$G = \sum_i \alpha_i^{(1)} C_i + \sum_{ij} \alpha_{ij}^{(2)} C_i C_j + \dots, \quad (7.8)$$

where the coefficients  $\alpha^{(m)}$  are of order  $m$  in curvature. There are in general  $(1+m)(1+m/2)$  coefficients of order  $m$ , but many are incompatible with the rotational symmetries of the proteins. To see this, we write Eq. (7.8) as a Fourier series

$$G = \sum_{n=0}^{\infty} a_{2n} \sin(2n\theta) + b_{2n} \cos(2n\theta). \quad (7.9)$$

The coefficients  $a_{2n}$  and  $b_{2n}$  are functions of  $H$  and  $D$ . Eqs. (7.8) and (7.9) relate to each other through trigonometric addition formulas [99]

$$\begin{aligned} D^n \sin(2n\theta) &= \sum_{k=0}^n \sin\left[\frac{\pi}{2}(n-k)\right] \binom{n}{k} C_2^k C_3^{n-k}, \\ D^n \cos(2n\theta) &= \sum_{k=0}^n \cos\left[\frac{\pi}{2}(n-k)\right] \binom{n}{k} C_2^k C_3^{n-k}. \end{aligned} \quad (7.10)$$

It follows that the lowest order terms in  $a_{2n}$  and  $b_{2n}$  are of order  $D^n$ . Since  $\theta$  enters the curvature tensor (7.3) through  $D \cos(2\theta)$  and  $D \sin(2\theta)$  terms, Eq. (7.8) contains only even terms. Also, for proteins in  $M$ -fold

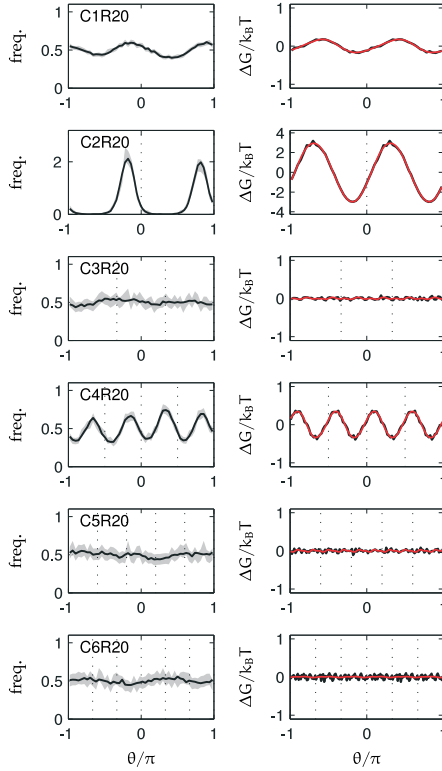


**Figure 7.8:** Orientational distributions on cylinders. (Left) Raw histograms of 1- to 6-mers in cylinders of radii  $R = 20\sigma$ , with aggregated distribution (black) and 95% bootstrapped confidence intervals (gray). (Right) Corresponding orientation free energy, where the symmetries of the cylinder and protein structures have been imposed to improve the statistics. Solid black lines are averages, and red lines are least-square fits of two-term Fourier series. Reprinted from Paper IV.

rotational symmetry, the orientation-dependent free energy should be invariant to the corresponding rotations

$$G(\theta) = G\left(\theta + \frac{2\pi}{M}\right), \quad (7.11)$$

which implies that Eq. (7.9) contains only terms where  $2n$  are multiples of  $M$ . Therefore, for  $M$ -mers with even  $M$ , the lowest order terms in  $G(\theta)$  are  $D^{M/2} \cos(M\theta)$  and  $D^{M/2} \sin(M\theta)$ , while for odd  $M$  they are  $D^M \cos(2M\theta)$  and  $D^M \sin(2M\theta)$ . As linear and/or quadratic terms are required for significant angular dependence at moderate curvatures, monomers, dimers and tetramers show orientation dependent curvature sensing in Fig. 7.8, while trimers, pentamers and hexamers do not.

Higher order terms should become relevant at higher curvatures. To test this, we ran a trimer simulation in a cylinder with radius  $R = 7\sigma$ . Here, the lowest order terms are  $D^3 \cos(6\theta)$  and  $D^3 \sin(6\theta)$ , so Eq. (7.9) predicts a 6-fold symmetric free energy profile. Fig. 7.9 shows that this is indeed the case. Although the trimer molecule is identical to that studied in Section 7.2, the change in membrane topology leads to some qualitative differences in the results. In the buckled membrane, the presence of a curvature gradient breaks the  $180^\circ$  rotation symmetry implied by Eq. (7.3), and thus we observe the trimer's 3-fold structural symmetry at the preferred curvature  $K_0 = 0.035 \sigma^{-1}$  on each side of the buckle. Cylindrical membranes have no curvature gradient, leading to the 6-fold symmetry just discussed, which is however not observable until the curvature  $K \gtrsim 0.1 \sigma^{-1}$  (Figs. 7.8, 7.9).

For moderate curvatures, our model predicts that the amplitude of the orientation dependent free energy for the tetramer should follow a purely quadratic law in curvature, while the monomer should also include a linear term. For both the monomer and the tetramer, Fig. 7.10 compares the amplitude of the free energy profiles for cylinders of varying radii, confirming this theoretical prediction.

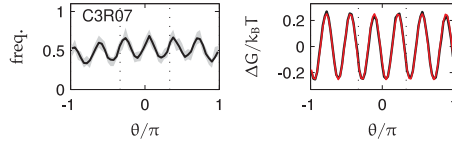


**Figure 7.9:** Shows the same functions as Fig. 7.8, but for the C3R07 simulation. As expected from Eqs. (7.9), (7.10), at sufficiently high curvatures, the free energy profile shows 6-fold symmetry. Adapted from Paper IV.

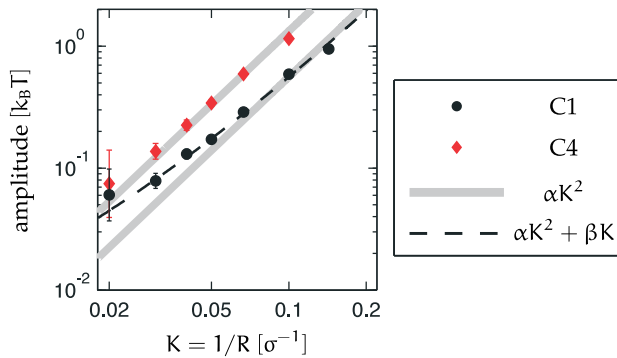


**Figure 7.10:** Curvature dependent rotation amplitudes. Theoretical expectation: The C1 protein amplitude follows a general quadratic dependence through the origin  $A_1 = \alpha K^2 + \beta K$ , while the C4 protein follows a pure square law  $A_4 \propto K^2$ . Adapted from Paper IV.



## 8. Conclusions

Membrane curvature sensing is a key factor in the shaping and spatial organization of biological cells and subcellular structures. Yet, both at the microscopic level of single molecules, and at the mesoscopic level where its effects are most apparent, we possess limited understanding. Molecular dynamics simulations offer a powerful avenue for research in this area, complementing biophysical experiments, though its impact has been limited in part due to the lack of efficient computational methods to deal with the methodological difficulties of analyzing simulated curved membranes. The majority of computational assays have relied on studying undulations in flat membrane patches, but these signals are weak and difficult to interpret.

Here we present a computational method to study curvature sensing. The method is based on simulated buckling, where the main signal is the position and orientation of a putative curvature sensing molecule along the curved membrane. These quantities can be directly related to the curvature-dependent binding free energy. A particular advantage of simulated buckling is that it presents a static and continuous range of curvature to the probes. Moreover, this range can include very high curvatures while simulating relatively small membrane patches. One of the main methodological challenges with this approach arises from the fact that the buckled membrane is subject to strong thermal fluctuations. Therefore, to be able to extract positional statistics of curvature sensors relative to the membrane, we developed a procedure which aligns each simulated frame to a theoretical shape. To evaluate the method, we perform a series of coarse-grained simulations, and show several of its features. The method is robust to noise, and is able to resolve signals not easily observable through other methods, including the nonlinear curvature dependence of lipid redistribution, and in-plane orientations of proteins. The two-component Cooke lipid system analyzed in Section 6.3 shows that coarse-grained lipids redistribute curved regions as expected from their geometry, in quantitative agreement with previous simulations of lipid vesicles. In Section 7.2, we

determined the curvature sensing properties of a model trimer which localizes to intermediate curvature. The presence of an intrinsic curvature preference is an important feature predicted by standard theoretical models, but that has proven difficult to actually observe. Moreover, we show that the trimer effectively senses the local curvature gradient, and not just the local curvature as usually assumed. A theory of sensing of curvature gradients is lacking, offering a particular focus for future work. As a buckled membrane is flat in the transverse direction, Gaussian curvature is everywhere zero (neglecting thermal undulations). This is a significant limitation, as some proteins are known to sense Gaussian curvature. An interesting avenue for further research is to generalize the method to shapes including Gaussian curvature by replacing the buckled shape parameterization.

In Chapter 6 we applied the buckling method to investigate three-component lipid membranes with varying concentrations of cardiolipin, which shows a strong preference for negative curvature, in agreement with experiments showing that it localizes to the cell poles in *E. Coli*. We calculated lipid order parameters, finding that the largest decrease occurs in regions of maximal negative curvature, consistent with a geometric mechanism for curvature sensing. In contrast with some theoretical predictions, we do not find a minimum concentration required for cardiolipin localization, because the simulated buckle probes high enough curvatures that curvature mismatch energies are high enough to localize single molecules. The curvature sensing properties of cardiolipin are essential to the understanding of several processes in mitochondria, as many proteins, including various respiratory complexes, bind to cardiolipin with high affinity and are stabilized by its presence. Similar calculations as those presented here could be performed to answer if and how cardiolipin facilitates protein localization within the inner mitochondrial membrane.

In curvature sensing and generation, the hydrophobic insertion mechanism is perhaps the most often discussed. Within our buckled membrane assay, it predicts amphipathic helices to localize to positive curvature, and to align to the flat direction [29, 97]. In Section 7.3 we studied the curvature sensing properties of three small amphipathic peptides. While they localize to positive curvature as expected, interestingly their orientational preferences differ, with none aligning in the expected direction perpendicular to the maximum curvature direction. Moreover, the orientation distributions do not show reflection symmetry, which

would be expected from shape-based effects. The actual peptide sequences break the symmetry, indicating a more complex underlying mechanism.

The buckling method can be applied to many other systems as well, including greater level of detail in atomistic simulations, although these are limited by computational resources. Enhanced sampling methods could alleviate this constriction. Metadynamics offers a promising path for further method development, where the probe's arc length position and in-plane orientation angle offer natural choices of collective variables to elucidate the free energy landscape of a curvature sensing assay.

Finally, in Section 7.4 turn to investigate orientation-dependent curvature sensing by rotationally symmetric multimers in cylindrical membranes. Through coarse-grained simulations and theoretical arguments we show that the structural symmetry of multimeric proteins plays an essential role in their ability to sense direction-dependent curvature. While monomers, dimers and tetramers show anisotropic curvature free energy profiles, orientation dependent curvature sensing is strongly suppressed by odd and higher order symmetries, suggesting a correlation between structural symmetry and biological function.



# A. Autocorrelation times

The autocorrelation time  $t_{ac}$ , defined as twice the exponential decay time [100] is

$$t_{ac} = 2t_{exp} = 2 \int_0^{\infty} dt \tilde{C}(t), \quad (\text{A.1})$$

where  $\tilde{C}(t)$  is the normalized autocorrelation function of each bin  $\hat{\rho}_i$  in a one-component system

$$C(t) = (\langle \hat{\rho}_i(t' + t)\hat{\rho}_i(t') \rangle - \langle \hat{\rho}_i \rangle^2) / (\langle \hat{\rho}_i^2 \rangle - \langle \hat{\rho}_i \rangle^2), \quad (\text{A.2})$$

averaged over all  $M$  bins and each lipid.  $\hat{\rho}$  is the single lipid midplane distribution, that is,  $\hat{\rho}_i(t) = 1$  if the lipid in question occupies bin  $i$  at time  $t$ , and  $\hat{\rho}_i(t) = 0$  otherwise (for a one-component bilayer,  $\langle \hat{\rho}_i \rangle \approx 1/M$ ).

Here we present the autocorrelation analysis for the Cooke one-component simulation and for the Martini allPE simulation in Chapter 6. As the autocorrelation time depends on lipid diffusion, we expect the results to be a reasonable approximations for all Martini and Cooke lipids, respectively, in the simulations presented in this work. Additionally we give estimated autocorrelation times for the trimer system of Section 7.2, and the multimers in Section 7.4.

From Fig. A.1b, we determine the autocorrelation time for the Cooke lipids to be  $t_{ac} = 2t_{exp} \approx 1090\tau$ . For the trimer system, we collected position data from a simulation of a trimer in a flat bilayer. The autocorrelation time of the trimer is estimated to be  $t_{ac} \approx 2.3 \times 10^5\tau$  based on this simulation data.

Following the same procedure, the autocorrelation time for the Martini lipids, calculated from the **allPE** simulation is estimated at  $t_{ac} = 2t_{exp} \approx 124\text{ns}$  (Fig. A.2b). In terms of the orientation angle  $\theta$ , estimates for the autocorrelation times for the multimers in Section 7.4 range from  $1.2 \times 10^3\tau$  for the monomer, to around  $8 \times 10^3\tau$  for the dimer, with the rest of the cases about  $5 \times 10^3\tau$ .

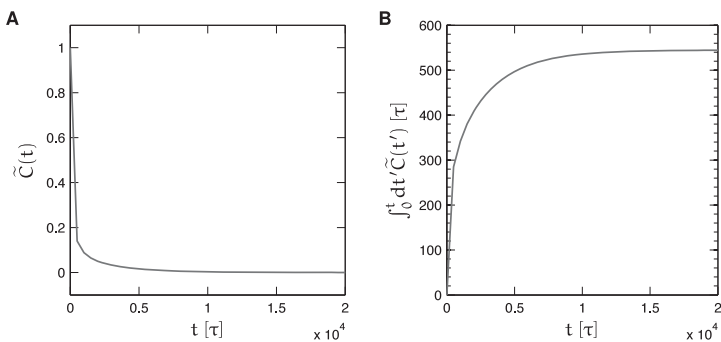


**Figure A.1:** (a) Normalized autocorrelation function  $\tilde{C}(t)$  for the one-component Cooke lipid system, with  $\gamma = 0.2$  (CC0.2 in Table 6.1). (b) Cumulative integral of  $\tilde{C}(t)$ , yielding the exponential decay time, Eq. (A.1). The autocorrelation time is  $t_{ac} = 2t_{exp} \sim 1090\tau$ . Reprinted with permission from Paper I. © 2018 ACS.

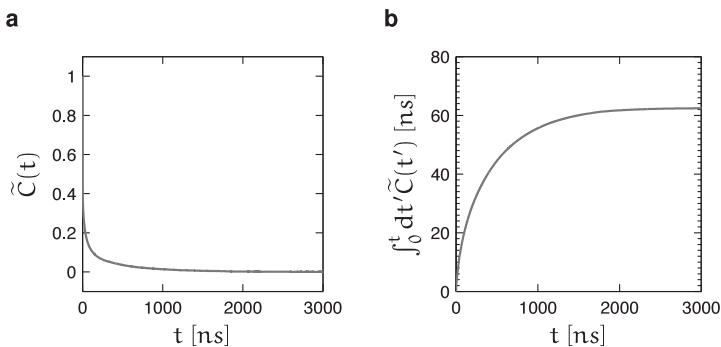


**Figure A.2:** (a) Normalized autocorrelation function  $\tilde{C}(t)$ . (b) The exponential decay time, given by  $t_{exp} = \int_0^\infty dt' \tilde{C}(t')$ . The autocorrelation time is  $t_{ac} = 2t_{exp} \sim 124$  ns. Data from the allPE simulation. Reprinted from Paper II.

# Sammanfattning

Krökningen hos cellmembran utgör en viktig drivkraft för att skapa och upprätthålla membranens form och sammansättning, genom mekanismer som låter membranbundna makomolekyler växelverka med den lokala krökningen hos membranen de binder till. De molekylära mekanismerna för krökningsberoende membranbindning är emellertid inte särskilt väl kända. Biomolekylära simuleringar kan utgöra ett komplement till experimentella studier av biomembran, men deras bidrag till förståelsen av krökningskänslighet har begränsats av metodologiska svårigheter att simulera deformerade membran. I den här avhandlingen utvecklar vi en metod baserad på mekanisk knäckning, som tidigare utnyttjas till att studera de mekaniska egenskaperna hos biomembran, till att studera krökningskänslighet. Vi beskriver utvärderar och validerar metoden, och tillämpar den för att studera krökningskänslighet hos modellsystem.

För lipiden cardiolipin, en komponent i mitokondrie-membran och vissa bakteriella membran, ser vi en preferens för negativ krökning som inte är beroende av kooperativa effekter eller växelverkan med andra krökningskänsliga molekyler. I en studie av korta amphipatiska peptider ser vi en preferens för positiv krökning, i kvalitativ överensstämmelse med tidigare teorier om hydrofob undanträngning när cylindriska inklusioner binder till membranets gränsskikt. Peptidernas konfigurationer i membranets plan fördelar sig dock mindre symmetriskt än man kunde förvänta sig av teorin för hydrofob undanträngning, vilket vi tolkar som en effekt av peptidernas osymmetriska molekylära struktur. Slutligen studerar vi förenklade modeller av symmetriska transmembranproteiner och relationen mellan proteinerstrukturers symmetri och deras krökningskänslighet. Vi ser en stark koppling, där möjligheten till anisotrop krökningskänslighet, dvs krökningskänslighet som beror av en molekyls riktning i membranets tangentplan, är starkt begränsad utom för osymmetriska molekyler samt två- och fyrfaldigt symmetriska proteiner.



# Acknowledgements

It is an immense privilege to be a PhD student at Stockholm University. I am thus extremely grateful to everyone who made that possible. To Martin Lindén, my original supervisor. You have always been extremely generous with your time. Even after fate sent us a curve ball, you went way above and beyond to take this project to fruition. To Erik Brandt, who did so much work for comparatively little credit to get this thesis to the finish line. Your enthusiasm and professionalism is contagious. And to Alexander Lyubartsev, supervisor supreme. Your help, amazing insight and generosity will not be forgotten.

I have greatly enjoyed my time at DBB and MMK, not in small part thanks to the people I spend my time with. To my office mates, Jordi, Inna, Bojan, Fredrik, Nikos, Diana. We have had a lot of laughs. To my lunch mates, Arnold, Erik, Sasha, Baltzar, Josef, Andrew, who provided fun and interesting conversation to make the everyday grind much more pleasant. To those whose name I forgot to include here, I am also grateful, and sorry for the slight.

Lastly, I would like to thank my gang and my family, for their continued friendship and support.



# References

- [1] T. Baumgart et al. Thermodynamics and mechanics of membrane curvature generation and sensing by proteins and lipids. *Annu. Rev. Phys. Chem.* **62**, 483 (2011).
- [2] B. J. Peter, H. M. Kent, I. G. Mills, Y. Vallis, P. J. G. Butler, P. R. Evans, and H. T. McMahon. Bar domains as sensors of membrane curvature: the amphiphysin bar structure. *Science* **303**, 495 (2004).
- [3] J. Bigay, J.-F. Casella, G. Drin, B. Mesmin, and B. Antonny. Arfgap1 responds to membrane curvature through the folding of a lipid packing sensor motif. *EMBO J.* **24**, 2244 (2005).
- [4] N. S. Hatzakis, V. K. Bhatia, J. Larsen, K. L. Madsen, P.-Y. Bolinger, A. H. Kunding, J. Castillo, U. Gether, P. Hedegård, and D. Stamou. How curved membranes recruit amphipathic helices and protein anchoring motifs. *Nat. Chem. Biol.* **5**, 835 (2009).
- [5] C. Prévost, H. Zhao, J. Manzi, E. Lemichez, P. Lappalainen, A. Callan-Jones, and P. Bassereau. Irsps53 senses negative membrane curvature and phase separates along membrane tubules. *Nat. Commun.* **6**, 8529 (2015).
- [6] A. A. Alnaas, C. L. Moon, M. Alton, S. M. Reed, and M. K. Knowles. Conformational changes in c-reactive protein affect binding to curved membranes in a lipid bilayer model of the apoptotic cell surface. *J. Phys. Chem. B* **121**, 2631 (2017).
- [7] A. J. Sodt and R. W. Pastor. Molecular modeling of lipid membrane curvature induction by a peptide: more than simply shape. *Biophys. J.* **106**, 1958 (2014).
- [8] M. Hu, P. Diggins IV, and M. Deserno. Determining the bending modulus of a lipid membrane by simulating buckling. *J. Chem. Phys.* **138**, 214110 (2013).
- [9] W. Helfrich. Elastic properties of lipid bilayers: theory and possible experiments. *Z. Naturforsch. C* **28**, 693 (1973).
- [10] A. N. Pressley. *Elementary differential geometry* (Springer Science & Business Media, 2010).
- [11] S. Antman. *Nonlinear Problems of Elasticity*. Applied Mathematical Sciences (Springer New York, 2005).
- [12] H. Noguchi. Anisotropic surface tension of buckled fluid membranes. *Phys. Rev. E* **83**, 061919 (2011).
- [13] G. Daum. Lipids of mitochondria. *BBA-Rev. Biomembranes* **822**, 1 (1985).
- [14] W. Dowhan. Genetic analysis of lipid-protein interactions in escherichia coli membranes. *BBA-Rev. Biomembranes* **1376**, 455 (1998).
- [15] A. J. Chicco and G. C. Sparagna. Role of cardiolipin alterations in mitochondrial dysfunction and disease. *Am. J. Physiol.-Cell Ph.* **292**, C33 (2007).

- [16] H. K. Saini-Chohan, M. G. Holmes, A. J. Chicco, W. A. Taylor, R. L. Moore, S. A. McCune, D. L. Hickson-Bick, G. M. Hatch, and G. C. Sparagna. Cardiolipin biosynthesis and remodeling enzymes are altered during development of heart failure. *J. Lipid Res.* **50**, 1600 (2009).
- [17] M. Schlame and M. Ren. Barth syndrome, a human disorder of cardiolipin metabolism. *FEBS Lett.* **580**, 5450 (2006).
- [18] S. M. Claypool and C. M. Koehler. The complexity of cardiolipin in health and disease. *Trends Biochem. Sci.* **37**, 32 (2012).
- [19] S. M. Claypool, Y. Oktay, P. Boontheung, J. A. Loo, and C. M. Koehler. Cardiolipin defines the interactome of the major ADP/ATP carrier protein of the mitochondrial inner membrane. *J. Cell. Bio.* **182**, 937 (2008).
- [20] D. Acehan, A. Malhotra, Y. Xu, M. Ren, D. L. Stokes, and M. Schlame. Cardiolipin affects the supramolecular organization of atp synthase in mitochondria. *Biophys. J.* **100**, 2184 (2011).
- [21] T. H. Haines and N. A. Dencher. Cardiolipin: a proton trap for oxidative phosphorylation. *FEBS Lett.* **528**, 35 (2002).
- [22] K. M. Davies, C. Anselmi, I. Wittig, J. D. Faraldo-Gómez, and W. Kühlbrandt. Structure of the yeast F<sub>1</sub>F<sub>o</sub>-ATP synthase dimer and its role in shaping the mitochondrial cristae. *Proc. Natl. Acad. Sci. USA* **109**, 13602 (2012).
- [23] L. D. Renner and D. B. Weibel. Cardiolipin microdomains localize to negatively curved regions of *Escherichia coli* membranes. *Proc. Natl. Acad. Sci. USA* **108**, 6264 (2011).
- [24] T. Romantsov, A. R. Battle, J. L. Hendel, B. Martinac, and J. M. Wood. Protein localization in *Escherichia coli* cells: comparison of the cytoplasmic membrane proteins ProP, LacY, ProW, AqpZ, MscS, and MscL. *J. Bacteriol.* **192**, 912 (2010).
- [25] T. Romantsov, S. Helbig, D. E. Culham, C. Gill, L. Stalker, and J. M. Wood. Cardiolipin promotes polar localization of osmosensory transporter ProP in *Escherichia coli*. *Mol. Microbiol.* **64**, 1455 (2007).
- [26] R. Mukhopadhyay, K. C. Huang, and N. S. Wingreen. Lipid localization in bacterial cells through curvature-mediated microphase separation. *Biophys. J.* **95**, 1034 (2008).
- [27] K. C. Huang, R. Mukhopadhyay, and N. S. Wingreen. A curvature-mediated mechanism for localization of lipids to bacterial poles. *PLOS Comput. Biol.* **2**, e151 (2006).
- [28] E. Strandberg, J. Zerweck, P. Wadhvani, and A. S. Ulrich. Synergistic insertion of antimicrobial magainin-family peptides in membranes depends on the lipid spontaneous curvature. *Biophys. J.* **104**, L9 (2013).
- [29] H. Cui, E. Lyman, and G. A. Voth. Mechanism of membrane curvature sensing by amphipathic helix containing proteins. *Biophys. J.* **100**, 1271 (2011).
- [30] H. T. McMahon and J. L. Gallop. Membrane curvature and mechanisms of dynamic cell membrane remodeling. *Nature* **438**, 590 (2005).
- [31] J. Zimmerberg and M. M. Kozlov. How proteins produce cellular membrane curvature. *Nat. Rev. Mol. Cell Bio.* **7**, 9 (2006).
- [32] Y. Shibata, J. Hu, M. M. Kozlov, and T. A. Rapoport. Mechanisms shaping the membranes of cellular organelles. *Annu. Rev. Cell Dev. Biol.* **25**, 329 (2009).

- [33] T. R. Graham and M. M. Kozlov. Interplay of proteins and lipids in generating membrane curvature. *Curr. Opin. Cell Biol.* **22**, 430 (2010).
- [34] R. Phillips, T. Ursell, P. Wiggins, and P. Sens. Emerging roles for lipids in shaping membrane-protein function. *Nature* **459**, 379 (2009).
- [35] A. Frost, V. M. Unger, and P. De Camilli. The BAR domain superfamily. *Cell* **137**, 191 (2009).
- [36] S. Howorka. Changing of the guard. *Science* **352**, 890 (2016).
- [37] J. C. Stachowiak, C. C. Hayden, and D. Y. Sasaki. Steric confinement of proteins on lipid membranes can drive curvature and tubulation. *Proc. Natl. Acad. Sci. USA* **107**, 7781 (2010).
- [38] M. M. Kozlov, F. Campelo, N. Liska, L. V. Chernomordik, S. J. Marrink, and H. T. McMahon. Mechanisms shaping cell membranes. *Curr. Opin. Cell Biol.* **29**, 53 (2014).
- [39] I. R. Cooke and M. Deserno. Coupling between lipid shape and membrane curvature. *Biophys. J.* **91**, 487 (2006).
- [40] M. M. Kamal, D. Mills, M. Grzybek, and J. Howard. Measurement of the membrane curvature preference of phospholipids reveals only weak coupling between lipid shape and leaflet curvature. *Proc. Natl. Acad. Sci. USA* **106**, 22245 (2009).
- [41] B. Sorre, A. Callan-Jones, J.-B. Manneville, P. Nassoy, J.-F. Joanny, J. Prost, B. Goud, and P. Bassereau. Curvature-driven lipid sorting needs proximity to a demixing point and is aided by proteins. *Proc. Natl. Acad. Sci. USA* **106**, 5622 (2009).
- [42] K. C. Huang and K. S. Ramamurthi. Macromolecules that prefer their membranes curvy. *Mol. Microbiol.* **76**, 822 (2010).
- [43] S. Vanni, L. Vamparys, R. Gautier, G. Drin, C. Etchebest, P. F. Fuchs, and B. Antonny. Amphipathic lipid packing sensor motifs: Probing bilayer defects with hydrophobic residues. *Biophys. J.* **104**, 575 (2013).
- [44] B. Sorre, A. Callan-Jones, J. Manzi, B. Goud, J. Prost, P. Bassereau, and A. Roux. Nature of curvature coupling of amphiphysin with membranes depends on its bound density. *Proc. Natl. Acad. Sci. USA* **109**, 173 (2012).
- [45] P. Ramesh, Y. F. Baroji, S. N. S. Reihani, D. Stamou, L. B. Oddershede, and P. M. Bendix. FBAR Syndapin 1 recognizes and stabilizes highly curved tubular membranes in a concentration dependent manner. *Sci. Rep.* **3**, 1565 (2013).
- [46] W.-T. Hsieh, C.-J. Hsu, B. R. Capraro, T. Wu, C.-M. Chen, S. Yang, and T. Baumgart. Curvature sorting of peripheral proteins on solid-supported wavy membranes. *Langmuir* **28**, 12838 (2012).
- [47] C. Zhu, S. L. Das, and T. Baumgart. Nonlinear sorting, curvature generation, and crowding of endophilin n-BAR on tubular membranes. *Biophys. J.* **102**, 1837 (2012).
- [48] H. M. Eriksson, P. Wessman, C. Ge, K. Edwards, and Å. Wieslander. Massive formation of intracellular membrane vesicles in *Escherichia coli* by a monotopic membrane-bound lipid glycosyltransferase. *J. Biol. Chem.* **284**, 33904 (2009).
- [49] J. C. Stachowiak, E. M. Schmid, C. J. Ryan, H. S. Ann, D. Y. Sasaki, M. B. Sherman, P. L. Geissler, D. A. Fletcher, and C. C. Hayden. Membrane bending by protein-protein crowding. *Nat. Cell Biol.* **14**, 944 (2012).

- [50] G. Drin, J.-F. Casella, R. Gautier, T. Boehmer, T. U. Schwartz, and B. Antony. A general amphipathic  $\alpha$ -helical motif for sensing membrane curvature. *Nat. Struct. Mol. Biol.* **14**, 138 (2007).
- [51] V. K. Bhatia, K. L. Madsen, P.-Y. Bolinger, A. Kunding, P. Hedegård, U. Gether, and D. Stamou. Amphipathic motifs in bar domains are essential for membrane curvature sensing. *EMBO J.* **28**, 3303 (2009).
- [52] N. Mizuno, J. Varkey, N. C. Kegulian, B. G. Hegde, N. Cheng, R. Langen, and A. C. Steven. Remodeling of lipid vesicles into cylindrical micelles by  $\alpha$ -synuclein in an extended  $\alpha$ -helical conformation. *J. Biol. Chem.* **287**, 29301 (2012).
- [53] A. R. Braun, E. Sevcsik, P. Chin, E. Rhoades, S. Tristram-Nagle, and J. N. Sachs.  $\alpha$ -synuclein induces both positive mean curvature and negative gaussian curvature in membranes. *J. Am. Chem. Soc.* **134**, 2613 (2012).
- [54] A. Tonnesen, S. M. Christensen, V. Tkach, and D. Stamou. Geometrical membrane curvature as an allosteric regulator of membrane protein structure and function. *Biophys. J.* **106**, 201 (2014).
- [55] N. W. Schmidt, A. Mishra, J. Wang, W. F. DeGrado, and G. C. Wong. Influenza virus a m2 protein generates negative gaussian membrane curvature necessary for budding and scission. *J. Am. Chem. Soc.* **135**, 13710 (2013).
- [56] S. Aimon, A. Callan-Jones, A. Berthaud, M. Pinot, G. E. Toombes, and P. Bassereau. Membrane shape modulates transmembrane protein distribution. *Dev. Cell* **28**, 212 (2014).
- [57] I. Arechaga, B. Miroux, S. Karrasch, R. Huijbregts, B. de Kruijff, M. J. Runswick, and J. E. Walker. Characterisation of new intracellular membranes in *Escherichia coli* accompanying large scale over-production of the b subunit of f(1)F(o) ATP synthase. *FEBS Lett.* **482**, 215 (2000).
- [58] K. Takei, V. I. Slepnev, V. Haucke, and P. De Camilli. Functional partnership between amphiphysin and dynamin in clathrin-mediated endocytosis. *Nat. Cell Biol.* **1**, 33 (1999).
- [59] A. Roux, G. Koster, M. Lenz, B. Sorre, J.-B. Manneville, P. Nassoy, and P. Bassereau. Membrane curvature controls dynamin polymerization. *Proc. Natl. Acad. Sci. USA* **107**, 4141 (2010).
- [60] J. L. Alejo, S. C. Blanchard, and O. S. Andersen. Small-molecule photostabilizing agents are modifiers of lipid bilayer properties. *Biophys. J.* **104**, 2410 (2013).
- [61] B. Antony. Mechanisms of membrane curvature sensing. *Annu. Rev. Biochem.* **80**, 101 (2011).
- [62] J. C. Black, P. P. Cheney, T. Campbell, and M. K. Knowles. Membrane curvature based lipid sorting using a nanoparticle patterned substrate. *Soft Matter* **10**, 2016 (2014).
- [63] P. Ferrand, P. Gasecka, A. Kress, X. Wang, F.-Z. Bioud, J. Duboisset, and S. Brasselet. Ultimate use of two-photon fluorescence microscopy to map orientational behavior of fluorophores. *Biophys. J.* **106**, 2330 (2014).
- [64] B. Hess, C. Kutzner, D. van der Spoel, and E. Lindahl. GROMACS 4. *J. Chem. Theory Comput.* **4**, 435 (2008).
- [65] M. J. Abraham, T. Murtola, R. Schulz, S. Páll, J. C. Smith, B. Hess, and E. Lindahl. Gromacs: High performance molecular simulations through multi-level parallelism from laptops to supercomputers. *SoftwareX* **1**, 19 (2015).

- [66] G. A. Tribello, M. Bonomi, D. Branduardi, C. Camilloni, and G. Bussi. PLUMED 2: new feathers for an old bird. *Comput. Phys. Commun.* **185**, 604 (2014).
- [67] D. E. King. Dlib-ml: A machine learning toolkit. *J. Mach. Learn. Res.* **10**, 1755 (2009).
- [68] MATLAB 2014a (The MathWorks Inc., Natick, Massachusetts, United States).
- [69] W. Humphrey, A. Dalke, and K. Schulten. VMD: Visual Molecular Dynamics. *J. Mol. Graphics* **14**, 33 (1996).
- [70] I. R. Cooke and M. Deserno. Solvent-free model for self-assembling fluid bilayer membranes: stabilization of the fluid phase based on broad attractive tail potentials. *J. Chem. Phys.* **123**, 224710 (2005).
- [71] J. D. Weeks, D. Chandler, and H. C. Andersen. Role of repulsive forces in determining the equilibrium structure of simple liquids. *J. Chem. Phys.* **54**, 5237 (1971).
- [72] I. Cooke, K. Kremer, and M. Deserno. Tunable generic model for fluid bilayer membranes. *Phys. Rev. E* **72**, 011506 (2005).
- [73] S. J. Marrink, A. H. De Vries, and A. E. Mark. Coarse grained model for semiquantitative lipid simulations. *J. Phys. Chem. B* **108**, 750 (2004).
- [74] S. J. Marrink, H. J. Risselada, S. Yefimov, D. P. Tieleman, and A. H. De Vries. The MARTINI force field: coarse grained model for biomolecular simulations. *J. Phys. Chem. B* **111**, 7812 (2007).
- [75] L. Monticelli, S. K. Kandasamy, X. Periole, R. G. Larson, D. P. Tieleman, and S.-J. Marrink. The MARTINI coarse-grained force field: extension to proteins. *J. Chem. Theory Comput.* **4**, 819 (2008).
- [76] X. Periole and S.-J. Marrink. The martini coarse-grained force field. In *Biomolecular Simulations*, pp. 533–565 (Springer, 2013).
- [77] G. Bussi, D. Donadio, and M. Parrinello. Canonical sampling through velocity rescaling. *J. Chem. Phys.* **126**, 014101 (2007).
- [78] U. Essmann, L. Perera, M. L. Berkowitz, T. Darden, H. Lee, and L. G. Pedersen. A smooth particle mesh ewald method. *J. Chem. Phys.* **103**, 8577 (1995).
- [79] B. J. Reynwar, G. Illya, V. A. Harmandaris, M. M. Muller, K. Kremer, and M. Deserno. Aggregation and vesiculation of membrane proteins by curvature-mediated interactions. *Nature* **447**, 461 (2007).
- [80] H. J. Risselada and S. J. Marrink. Curvature effects on lipid packing and dynamics in liposomes revealed by coarse grained molecular dynamics simulations. *Phys. Chem. Chem. Phys.* **11**, 2056 (2009).
- [81] V. A. Harmandaris and M. Deserno. A novel method for measuring the bending rigidity of model lipid membranes by simulating tethers. *J. Chem. Phys.* **125**, 204905 (2006).
- [82] R. Parthasarathy, C.-h. Yu, and J. T. Groves. Curvature-modulated phase separation in lipid bilayer membranes. *Langmuir* **22**, 5095 (2006).
- [83] E. G. Brandt and A. P. Lyubartsev. Molecular dynamics simulations of adsorption of amino acid side chain analogues and a titanium binding peptide on the TiO<sub>2</sub> (100) surface. *J. Phys. Chem. C* **119**, 18126 (2015).

- [84] J. C. Gower and G. B. Dijksterhuis. *Procrustes problems*, vol. 30 (Oxford University Press on Demand, 2004).
- [85] S. Bhattacharya and S. Haldar. Interactions between cholesterol and lipids in bilayer membranes. role of lipid headgroup and hydrocarbon chain-backbone linkage. *BBA-Biomembranes* **1467**, 39 (2000).
- [86] E. Mileykovskaya and W. Dowhan. Cardiolipin membrane domains in prokaryotes and eukaryotes. *BBA-Biomembranes* **1788**, 2084 (2009).
- [87] K. J. Boyd, N. N. Alder, and E. R. May. Buckling under pressure: curvature-based lipid segregation and stability modulation in cardiolipin-containing bilayers. *Langmuir* **33**, 6937 (2017).
- [88] J. Fournier. Nontopological saddle-splay and curvature instabilities from anisotropic membrane inclusions. *Phys. Rev. Lett.* **76**, 4436 (1996).
- [89] N. Ramakrishnan, P. S. Kumar, and J. H. Ipsen. Monte carlo simulations of fluid vesicles with in-plane orientational ordering. *Phys. Rev. E* **81**, 041922 (2010).
- [90] K. Akabori and C. D. Santangelo. Membrane morphology induced by anisotropic proteins. *Phys. Rev. E* **84**, 061909 (2011).
- [91] N. Ramakrishnan, P. B. Sunil Kumar, and J. H. Ipsen. Membrane-mediated aggregation of curvature-inducing nematogens and membrane tubulation. *Biophys. J.* **104**, 1018 (2013).
- [92] Š. Perutková, V. Kralj-Iglič, M. Frank, and A. Iglič. Mechanical stability of membrane nanotubular protrusions influenced by attachment of flexible rod-like proteins. *J. Biomech.* **43**, 1612 (2010).
- [93] N. Ramakrishnan, P. Kumar, and J. H. Ipsen. Modeling anisotropic elasticity of fluid membranes. *Macromol. Theor. Simul.* **20**, 446 (2011).
- [94] T. Hara, H. Kodama, M. Kondo, K. Wakamatsu, A. Takeda, T. Tachi, and K. Matsuzaki. Effects of peptide dimerization on pore formation: Antiparallel disulfide-dimerized magainin 2 analogue. *Biopolymers* **58**, 437 (2001).
- [95] T. C. Terwilliger, L. Weissman, and D. Eisenberg. The structure of melittin in the form i crystals and its implication for melittin's lytic and surface activities. *Biophys. J.* **37**, 353 (1982).
- [96] G. Wang. Structures of human host defense cathelicidin ll-37 and its smallest antimicrobial peptide kr-12 in lipid micelles. *J. Biol. Chem.* **283**, 32637 (2008).
- [97] F. Campelo, H. T. McMahon, and M. M. Kozlov. The hydrophobic insertion mechanism of membrane curvature generation by proteins. *Biophys. J.* **95**, 2325 (2008).
- [98] D. S. Goodsell and A. J. Olson. Structural symmetry and protein function. *Annu. Rev. Bioph. Biom.* **29**, 105 (2000).
- [99] E. W. Weisstein. Multiple-Angle Formulas. From MathWorld—A Wolfram Web Resource). <http://mathworld.wolfram.com/Multiple-AngleFormulas.html>.
- [100] B. A. Berg and A. Billoire. *Markov chain Monte Carlo simulations* (Wiley Online Library, 2008).